Economic Geology, v. 117, no. 7, pp. 1573–1596

High-Grade Copper and Gold Deposited During Postpotassic Chlorite-White Mica-Albite Stage in the Far Southeast Porphyry Deposit, Philippines

Michael F. Calder,[1,†,*] Zhaoshan Chang,[1,**] Antonio Arribas,[2] Alina Gaibor,[3,***] Peter Dunkley,[3,***] Jeffrey Pastoral,[3] Kalin Kouzmanov,[4] Carl Spandler,[1,****] and Jeffrey W. Hedenquist[5]

[1]*Economic Geology Research Centre (EGRU), James Cook University, Townsville, Queensland 4811, Australia*

[2]*Department of Earth, Environmental and Resource Sciences, The University of Texas at El Paso, Texas 79968, USA*

[3]*Far Southeast Gold Resources, Inc., 8749 Paseo de Roxas, Makati, Philippines*

[4]*Department of Earth Sciences, University of Geneva, CH-1205 Geneva, Switzerland*

[5]*Department of Earth and Environmental Science, University of Ottawa, Ontario K1N 6N5, Canada*

Abstract

Ninety-eight underground diamond holes (~102 km) drilled by Far Southeast Gold Resources Inc. at the Far Southeast porphyry Cu-Au deposit, Philippines, from 2011 to mid-2013, provide a three-dimensional exposure of the deposit between 700- and –750-m elevation, with surface at ~1,400-m elevation. Far Southeast contains an inferred resource of 891.7 million tonnes (Mt) averaging 0.7 g/t Au and 0.5 wt % Cu, equivalent to 19.8 Moz Au and 4.5 Mt Cu. This contribution reports the spatial and temporal distribution of alteration and mineralization at Far Southeast, notably a white-mica–chlorite-albite assemblage that formed after early secondary biotite and before late quartz–white-mica–pyrite alteration and that is associated with the highest copper and gold grades.

Alteration assemblages were determined by drill core logging, short-wavelength infrared (SWIR) spectral analysis, petrographic examination, and a quantitative evaluation of materials by scanning electron microscopy (QEMSCAN) study. Alteration is limited around sparse veins or pervasive where vein density is high and the alteration halos coalesce. The alteration and mineralization zones with increasing depth are as follows: (1) the lithocap of quartz-alunite–dominated advanced argillic-silicic alteration that hosts part of the Lepanto high-sulfidation Cu-Au epithermal deposit (mostly above ~700-m elevation), (2) an aluminosilicate-dominated zone with coexisting pyrophyllite-diaspore ± kandite ± alunite and white mica (~700- to ~100-m elevation), (3) porphyry-style assemblages characterized by stockwork veins (below ~500-m elevation), (4) the 1 wt % Cu equivalent ore shell (~400- to –300-m elevation), and (5) an underlying subeconomic zone (about –300- to –750-m elevation, the base of drilling). The ore shells have a typical bell shape centered on a dioritic intrusive complex.

The paragenetic sequence of the porphyry deposit includes stage 1 granular gray to white quartz-rich (± anhydrite ± magnetite ± biotite) veins with biotite-magnetite alteration. These were cut by stage 2 lavender-colored euhedral quartz-rich (± anhydrite ± sulfides) veins, with halos of greenish white-mica–chlorite-albite alteration. The white mica is largely illite, with an average 2,203-nm Al-OH wavelength position. The albite may reflect the mafic nature of the diorite magmatism. The quartz veins of this stage are associated with the bulk of copper deposited as chalcopyrite and bornite, as well as gold. Thin Cu sulfide (chalcopyrite, minor bornite) veins with minor quartz and/or anhydrite (paint veins), with or without a white-mica halo, also occur. These veins were followed by stage 3 anhydrite-rich pyrite-quartz veins with white-mica (avg 2,197 nm, illite)–pyrite alteration halos.

Combined with previous studies, we conclude that this porphyry system, including the Far Southeast porphyry and Lepanto high-sulfidation Cu-Au deposits, evolved over a period of 0.1–0.2 m.y. Three diorite porphyry stocks were emplaced, and by ~1.4 Ma biotite-magnetite–style alteration formed with quartz-anhydrite veins and deposition of ≤0.5% Cu and ≤0.5 g/t Au (stage 1); coupled with this alteration style, a barren lithocap of residual quartz with quartz-alunite halo plus kandite ± pyrophyllite and/or diaspore formed at shallower depth (>700-m elevation). Subsequently, lavender quartz and anhydrite veins with bornite and chalcopyrite (high-grade stage, avg ~1 wt % Cu and ~1 g/t Au) and white-mica–chlorite-albite halos formed below ~400-m elevation (stage 2). They were accompanied by local pyrite replacement, the formation of hydrothermal breccias and Cu sulfide (paint) veins. Stage 2 was followed at ~1.3 Ma by the formation of igneous breccias largely along the margins of the high-grade zones and stage 3 pyrite-quartz-anhydrite ± chalcopyrite veins with white-mica (mostly illitic) halos. At shallower depths in the transition to the base of the lithocap, cooling led to the formation of aluminosilicate minerals (mainly pyrophyllite ± diaspore ± dickite) with anhydrite plus high-sulfidation-state sulfides and pyrite veinlets. Consistent with previous studies, it is likely that the lithocap-hosted enargite-Au mineralization formed during this later period.

[†]Corresponding author: e-mail, michael.f.calder@gmail.com
[*]Present address: 42 rue de Zurich, 1201 Geneva, Switzerland.
[**]Present address: Department of Geology and Geological Engineering, Colorado School of Mines, Golden, Colorado 80401, USA.
[***]Present address: Riverside Cottage, The Parade, Lostwithiel, Cornwall PL22 0DY, United Kingdom.
[****]Present address: Department of Earth Sciences, The University of Adelaide, South Australia 5005, Australia.

Introduction

Porphyry copper systems, which include porphyry deposits, account for about three-quarters of global copper, half of molybdenum, and about one-fifth of gold production (Sillitoe, 2010). However, the majority of porphyry deposits that crop

ISSN 0361-0128; doi:10.5382/econgeo.4940; 24 p.
Digital appendices are available in the online Supplements section.

Submitted: May 10, 2021 /Accepted: January 12, 2022

out have been discovered, requiring deeper exploration (Arndt et al., 2017), meaning that knowing and understanding alteration signatures and zonation, particularly toward deeper levels, is crucial to improve exploration efficiency and success. This study examines the alteration and ore paragenesis and zoning of the Far Southeast porphyry Cu-Au deposit, northern Luzon, Philippines, which lies ~1 km below surface (Fig. 1) and is in an advanced exploration stage (Gold Fields, 2019).

The Far Southeast porphyry deposit was discovered in 1980 (Concepcion and Cinco, 1989), subjacent to a lithocap (Sillitoe, 1995) of residual quartz with a quartz-alunite alteration halo that hosts the Lepanto enargite-gold deposit (Fig. 1B; Gonzalez, 1959; Claveria, 2001). Mining of the Lepanto deposit between 1938 and 1996 produced 36.3 million tonnes (Mt) of ore at 2.9 wt % Cu, 3.4 g/t Au, and 14 g/t Ag, with recovery of 3.2 Moz Au, 13.8 Moz Ag, and 0.74 Mt Cu (Chang et al., 2011). The discovery histories of both deposits, plus that of the adjacent Victoria epithermal veins (initial resource of 11 Mt at 7.3 g/t Au), were reviewed by Chang et al. (2011). From 2010 to mid-2013, the Far Southeast Gold Resources, Inc. (FSGRI) company, a joint venture between Gold Fields Limited and Lepanto Consolidated Mining Company, drilled over 102 km of diamond core in 98 new holes collared underground from numerous cuddies at 700-m elevation, about 700 m below the surface (Gaibor et al., 2013). This work established an inferred resource of 891.7 Mt of ore at 0.7 g/t Au and 0.5% Cu (Gold Fields, 2019), with the top of the resource at ~400-m elevation (1 km below the present surface) and the base at about –200- to –500-m elevation. The availability of the deep drill core provided the opportunity to document a complete world-class porphyry copper deposit over a vertical interval of ~1.5 km.

Previous studies of the Lepanto epithermal deposit and its host lithocap demonstrated a temporal and genetic linkage with the deeper Far Southeast porphyry deposit (Arribas et al., 1995; Hedenquist et al., 1998). Lepanto is located northwest of the porphyry deposit and its associated quartz diorite intrusions (Fig. 1B; Chang et al., 2011; Hedenquist et al., 2017). The historical alteration sequence described at Far Southeast includes potassic alteration followed by sericite-clay-chlorite and final sericite-dominant assemblages. Pyrophyllite-dominant assemblages occur at shallower elevations in the transition to the Lepanto epithermal deposit (Hedenquist et al., 1998, and references therein). Evidence that much of the copper and gold in the Far Southeast deposit was precipitated during formation of the postpotassic white-mica alteration was presented by Hedenquist et al. (1998), who also noted that the hydrothermal fluids responsible for these alteration stages were magmatic in origin.

In this study, we focused on the evolution of crosscutting veins, their mineralogy, and associated alteration halos. Drill core observations were made from the base of the lithocap at ~700-m depth, through a transition zone hundreds of meters thick to the top and through the porphyry ore zone, to the low-grade roots at –750-m elevation, more than 2 km below the present surface at 1,400-m elevation. Mineralogical observations consisted of core logging, a petrographic study, and microprobe, short-wavelength infrared (SWIR) and quantitative evaluation of minerals by scanning electron microscopy (QEMSCAN) analyses provided a 3-D characterization of the deposit, which contributed to our genetic interpretations.

General Mineralogical Features of Porphyry Deposits

Knowledge of porphyry copper deposits has accumulated for nearly 100 years, with the fundamental geologic elements and ore environments of porphyry deposits known by the 1930s (Lindgren, 1933). Lowell and Guilbert (1970) recognized common zonation patterns of porphyry copper deposits, and Gustafson and Hunt (1975) published a detailed study of alteration at the El Salvador, Chile, porphyry copper deposit; they introduced the Anaconda mining company's observations of the different styles of veins and the time sequence of various zoning patterns, from early and hot to later and cooler and generated in conditions of either lithostatic or hydrostatic pressure, respectively. Recent reviews of porphyry copper deposits have focused on the overall architecture of the alteration/mineralization system (Sillitoe, 2010) and on the nature of the magmas and hydrothermal fluids involved (Audétat and Simon, 2012; Kouzmanov and Pokrovski, 2012; Audétat, 2019).

Various alteration types (mineral assemblages related to vein types originally defined by Gustafson and Hunt, 1975) are typically present in porphyry copper systems associated with calc-alkaline arc magmas (summarized by Seedorff et al., 2005, 2008; Sillitoe, 2010, and references therein). Sodic-calcic alteration is located on the deep margin, below the ore zone, and is composed of albite-actinolite-magnetite as halos of magnetite ± actinolite (M) veinlets. Sodic alteration is located deep, proximal to the ore zone, up to the level of white-mica alteration and consists of albite-chlorite-epidote ± specularite, commonly as halos of quartz-pyrite-tourmaline veins. Propylitic alteration occurs on deposit margins with variable amounts of Fe-rich amphibole-epidote-chlorite-pyrite ± albite ± carbonate. Sodic-calcic, sodic, and propylitic alteration types are typically barren. Potassic alteration is located deep, in the core of the ore deposit with magnetite-biotite ± K-feldspar, as halos of quartz-magnetite-biotite ± anhydrite ± Cu sulfide (A) veins and coincident with many ore zones. Paragenetically later chlorite–white-mica alteration is located in the upper portions of the deposit core with quartz-sulfide veins (pyrite, chalcopyrite) and remnant magnetite, martite, or specularite ± anhydrite and is commonly associated with ore minerals. White-mica alteration is common as quartz–white-mica ± pyrite halos to quartz-pyrite (D) veins and locally with upward increase in chalcopyrite, tennantite, and enargite abundance (Gustafson and Hunt, 1975). Sericitic and phyllic are synonyms of white mica; however, Meyer and Hemley (1967) advocated for the mineralogy to be determined and use of the term sericite to be discontinued.

Transitional to the epithermal environment, above the porphyry ore zone, aluminosilicate alteration (pyrophyllite-diaspore ± kandite ± alunite) typically cuts white mica, locally with shallow pyrite and traces of high-sulfidation-state sulfides. A lithocap occurs at shallow levels, up to the paleosurface, and can be a flat-lying body consisting of a core of residual quartz, with advanced argillic alteration halos of quartz-alunite outward to kandite (kaolinite and/or dickite), locally with pyrophyllite and/or diaspore in feeder structures. Lithocaps form

over porphyry deposits (Sillitoe, 1995, 1999) at the time of deep potassic alteration (Arribas et al., 1995), which can be explained by the linkage between vapor and hypersaline liquid, respectively (Henley and McNabb, 1978). The lithocap is barren on formation (Chang et al., 2011; Hedenquist and Taran, 2013) but is a potential host for the introduction of subsequent intermediate- to high-sulfidation-state sulfides and gold (Hedenquist et al., 1998, 2000; Sillitoe and Hedenquist, 2003).

In some porphyry Cu deposits, such as Bajo de Alumbrera, Argentina, the highest metal grades appear to be associated

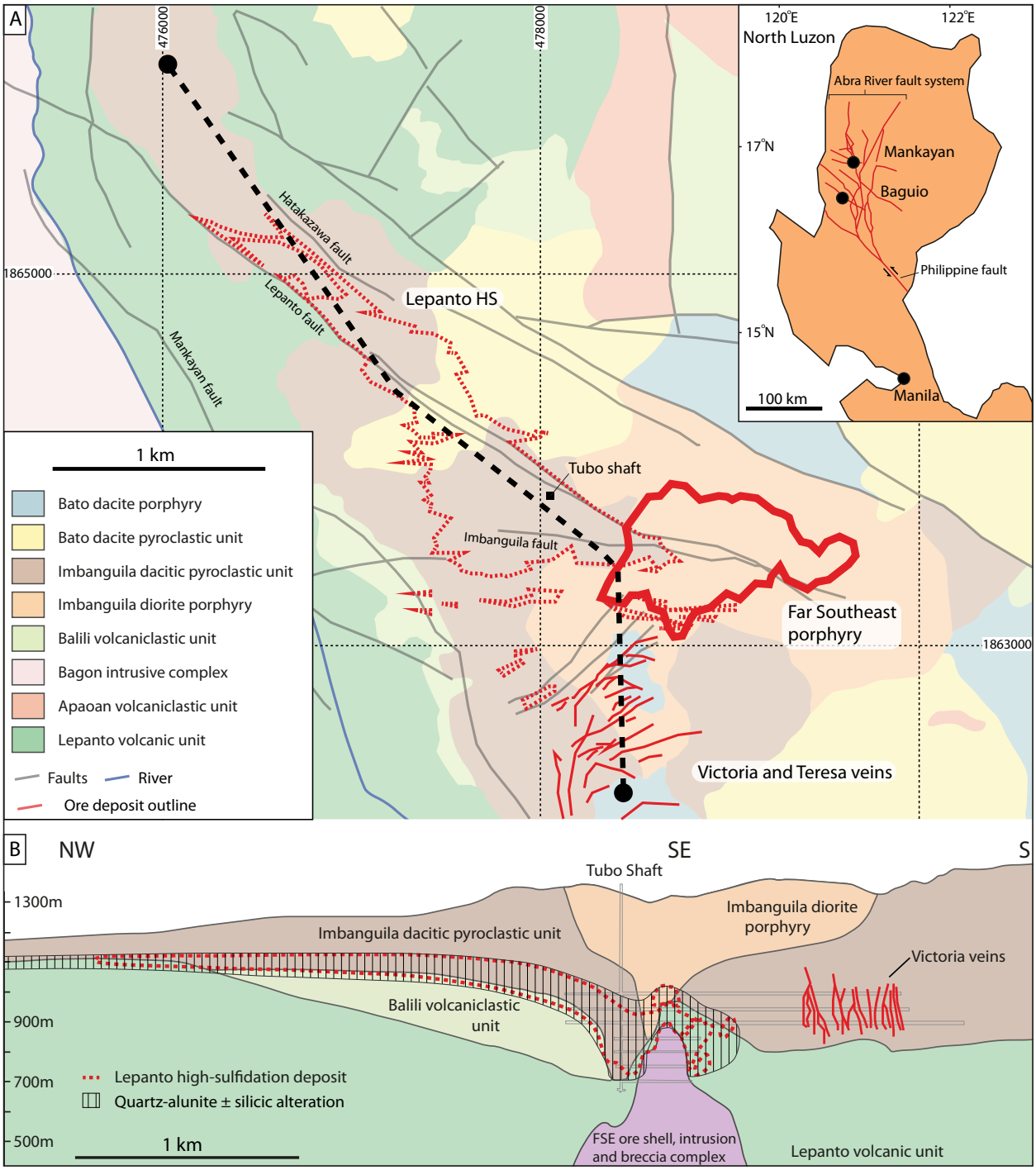

Fig. 1. A. Geologic map of the Mankayan district showing volcanic units (modified from Chang et al., 2011). The surface projection of the Lepanto high-sulfidation (HS) epithermal, Far Southeast (FSE) porphyry, and intermediate-sulfidation Victoria veins are shown. A 6-km longitudinal section across the district is shown by dashed line, turning north-south to be a cross section in the vicinity of the Victoria veins (Fig. 1B). PRS 92 UTM grid datum. B. Schematic northwest-southeast, north-south long and cross section through the Lepanto enargite-Au high-sulfidation epithermal deposit, the FSE porphyry deposit, and the intermediate-sulfidation Victoria veins (see trace in Fig. 1A; Chang et al., 2011).

with the early period of potassic alteration (Proffett, 2003). In contrast, there is evidence for copper and gold deposition to occur subsequent to biotite alteration, including at Chuquicamata and Escondida, Chile (Ossandón et al., 2001; Padilla-Garza et al., 2004), Butte, United States (Reed et al., 2013, and references therein), Batu Hijau, Indonesia (Clode et al., 1999; Garwin, 2002; Arif and Baker, 2004), and Pebble, Alaska (Lang and Gregory, 2012; Gregory, 2017). Sillitoe (2010) noted that chlorite–white-mica (sericite) alteration (Sillitoe and Gappe, 1984) is prevalent in the shallower parts of some porphyry Cu deposits, particularly those that are gold rich, and overprints preexisting potassic assemblages, with magnetite converted to hematite, and pyrite plus chalcopyrite deposited. Although copper and/or gold tenors of the former potassic zones may undergo depletion during the chlorite–white-mica overprint (e.g., Esperanza, northern Chile; Perelló et al., 2004), metal introduction is also recognized, such as at Escondida and Rosario, Chile (Padilla-Garza et al., 2001; Masterman et al., 2005). Indeed, this type of alteration at a few deposits is considered to account for much of the contained copper (e.g., Cerro Colorado, northern Chile; Bouzari and Clark, 2006).

Consistent with this recognition, cathodoluminescence (CL) imaging also indicates that early quartz veins that formed at high temperature are typically reopened and filled by quartz and copper sulfides at lower temperature, e.g., at Butte (Rusk and Reed, 2002), as well as at Bingham Canyon (Redmond et al., 2004; Redmond and Einaudi, 2010) and Santa Rita (Tsuruoka et al., 2021), United States, plus at El Salvador (Watanabe et al., 2018). In some cases, copper precipitation is not accompanied by quartz deposition (i.e., sulfide-only veinlets of chalcopyrite or bornite, referred to as paint veins by some; e.g., Stefanova et al., 2014), due to the fluid being within the field of retrograde solubility of quartz at ~380°–550°C (Fournier, 1985; Shock et al., 1989), overlapping with the temperature of copper deposition at Bingham Canyon (350°–420°C; Landtwing et al., 2005).

Geology, Geochronology, and Structure of the Mankayan District

The Far Southeast porphyry deposit is located in the Mankayan district of the Cordillera Central of northern Luzon (Fig. 1A). The N-trending Philippine archipelago is flanked by two convergent zones, the Manila trench to the west and the Philippine trench to the east (Queano et al., 2007; Hollings et al., 2011). When mineralization occurred at 2–1 Ma in the Mankayan district, eastward subduction of the aseismic Scarborough sea ridge beneath the region was ongoing (Cooke et al., 2005).

The geology of the district has been described by Gonzalez (1959), Sillitoe and Angeles (1985), Concepción and Cinco (1989), Garcia (1991), and Chang et al. (2011). More recent geologic mapping by FSGRI (P. Dunkley, unpub. report, 2015) has refined the stratigraphy, which comprises a basement of pre-middle Miocene volcanic and intrusive rocks, overlain by a cover sequence of Pleistocene dacitic tuffs and breccias intruded by domes that are broadly andesitic in composition. The Pleistocene volcanism was accompanied by the shallow intrusion of diorite complexes (within only a few kilometers of the paleosurface), with which the mineralization in the district is related (Fig. 1B).

Data for recent radiometric dating results (Table 1; P. Dunkley, unpub. report, 2015) are presented in the digital Appendix Table A1, including methods. The oldest exposed stratigraphic unit, the Lepanto volcanic unit, comprises a thick sequence of basaltic pillow lavas, hyaloclastites, and tuffaceous rocks, with a minor rhyolitic component toward the top, and was intruded by basaltic and rhyolitic dikes. Uranium-Pb zircon dates of 35.3 ± 1.0 and 33.7 ± 0.7 Ma have been obtained for the rhyolites (Table 1; P. Dunkley, unpub. report, 2015). Uncertainties listed for dates are all at 2σ or 95% confidence level. A large gabbro-diorite-tonalite pluton, the Bagon complex, dated by U-Pb on zircons at 34.8 ± 0.7 and 34.5 ± 0.5 Ma (Table 1; P. Dunkley, unpub. report, 2015), intruded the Lepanto volcanic

Table 1. Recent Radiometric Dates for the Far Southeast Area (Dunkley, 2015)

Sample	Easting	Northing	Rock unit	Rock type	Method	Date (Ma)
PNDLP1482	265716	1866367	Lepanto volcanic unit	Rhyolite	Zircon U-Pb LA-ICP-MS	33.69 ± 0.7
PNDLP1713	264394	1861679	Lepanto volcanic unit	Rhyolite	Zircon U-Pb LA-ICPMS	35.27 ± 1.0
PNDLP1633	262453	1862855	Bagon intrusive complex	Tonalite	Zircon U-Pb LA-ICP-MS	34.51 ± 0.5
PNDLP1672	262098	2867937	Bagon intrusive complex	Tonalite	Zircon U-Pb LA-ICP-MS	34.75 ± 0.7
PNDLP1712	266901	1863805	Imbanguila diorite	Diorite	Plagioclase Ar-Ar	1.94 ± 0.3
FSU11-2007-710.34–710.41	FSE drill hole		FSE porphyry	Quartz-anhydrite-molybdenite vein	Molybdenite Re-Os	1.48 ± 0.01
FSU11-7018A 815.56–815.62	FSE drill hole		FSE porphyry	Quartz-anhydrite-molybdenite vein	Molybdenite Re-Os	1.50 ± 0.01
PNDLP1604	267573	1863191	Bato intrusion	High-Si andesite	Groundmass plagioclase Ar-Ar	1.53 ± 0.2
PNDLP1670	266463	1860417	Bato intrusion	Dacite	Groundmass plagioclase Ar-Ar	1.16 ± 0.1
FSS11-145.5–145.68	Madaymen geotechnical drill hole for ventilation shaft		Bato intrusion	High-Si andesite	Groundmass plagioclase Ar-Ar	1.68 ± 0.3

Notes: Easting and Northing coordinates are in UTM zone 51N; datum: Luzon Philippines; data for all dates, as well as methodologies, are listed in the digital Appendix

FSE = Far Southeast, LA-ICP-MS = laser ablation-inductively coupled plasma-mass spectrometry

unit and forms part of the more extensive Central Cordillera batholith that runs along the spine of the Luzon Cordillera Central. The Balili volcaniclastic unit unconformably overlies the Lepanto volcanic unit and consists of poorly sorted epiclastic volcanic breccias, conglomerates, and sandstones. The breccias and conglomerates are mainly composed of polymictic clasts of andesite, minor clasts of diorite and granite, and rare clasts of limestone. Based on fossil evidence, Maleterre (1989) assigned a late Oligocene-early Miocene age to the Balili unit.

The Pleistocene volcanic sequence comprises the Imbanguila pyroclastic unit overlain by the Bato pyroclastic unit. Both units consist of massive to poorly stratified dacitic tuff breccias and fine tuffs containing beds with accretionary lapilli. The tuff breccias and tuffs contain lithic blocks and lapilli of diverse composition, including widespread clasts of diorite with porphyry-style veinlets and mineralization (Sillitoe, 1983; P. Dunkley, unpub. report, 2015). The Imbanguila unit is a host to the Lepanto enargite orebody and is widely affected by strong alteration. It is intruded by the Imbanguila diorite porphyry (also known as Imbanguila dacite porphyry), which has yielded K-Ar hornblende dates from 2.19 ± 0.62 to 1.82 ± 0.36 Ma (Arribas et al., 1995) and an Ar-Ar date on groundmass plagioclase of 1.94 ± 0.26 Ma (Table 1; P. Dunkley, unpub. report, 2015). The younger Bato units are syn- to postmineralization in age and less affected by hydrothermal alteration. Arribas et al. (1995) obtained a K-Ar date of 1.43 ± 0.21 Ma on hornblende from the matrix of a Bato tuff breccia. Numerous domes and laccoliths of broadly dacitic composition that intruded the Bato pyroclastic sequence at shallow depth yielded biotite and hornblende K-Ar dates of 1.18 ± 0.08 and 0.96 ± 0.29 Ma, respectively (Arribas et al., 1995) and Ar-Ar dates on groundmass plagioclase ranging from 1.68 ± 0.33 to 1.16 ± 0.09 Ma (Table 1; P. Dunkley, unpub. report, 2015).

The structure of the district is dominated by a complex zone of N- to NW-trending faults of the Abra River fault system (Fig. 1A), which is the main branch of the Philippine fault running along the length of the Luzon Cordillera Central (Barrier et al., 1991). Geologic mapping by FSGRI shows the NW-trending Mankayan fault is a major strand of the system and the largest fault in the district. Northwest- and E-trending secondary faults (Lepanto, Hatakazawa, and Imbanguila faults; Fig. 1A) splay from the Mankayan fault and were primary controls on the emplacement of the enargite lodes of the Lepanto mine as well as the Far Southeast porphyry deposit.

The E-trending Imbanguila fault coincides with a strong E-trending gravity gradient, interpreted as a deep-rooted basement structure thought to have controlled the emplacement of the Far Southeast intrusive complex, the main host of the Far Southeast porphyry Cu-Au deposit (Gaibor et al., 2013; Fig. 2). The Far Southeast complex consists of several diorite bodies that intruded the Lepanto volcanic unit and the Imbanguila diorite porphyry, which are cut across by large pipe-like breccia bodies (Fig. 2). Hydrothermal biotite from the Far Southeast deposit reported an average K-Ar date of 1.41 ± 0.05 Ma

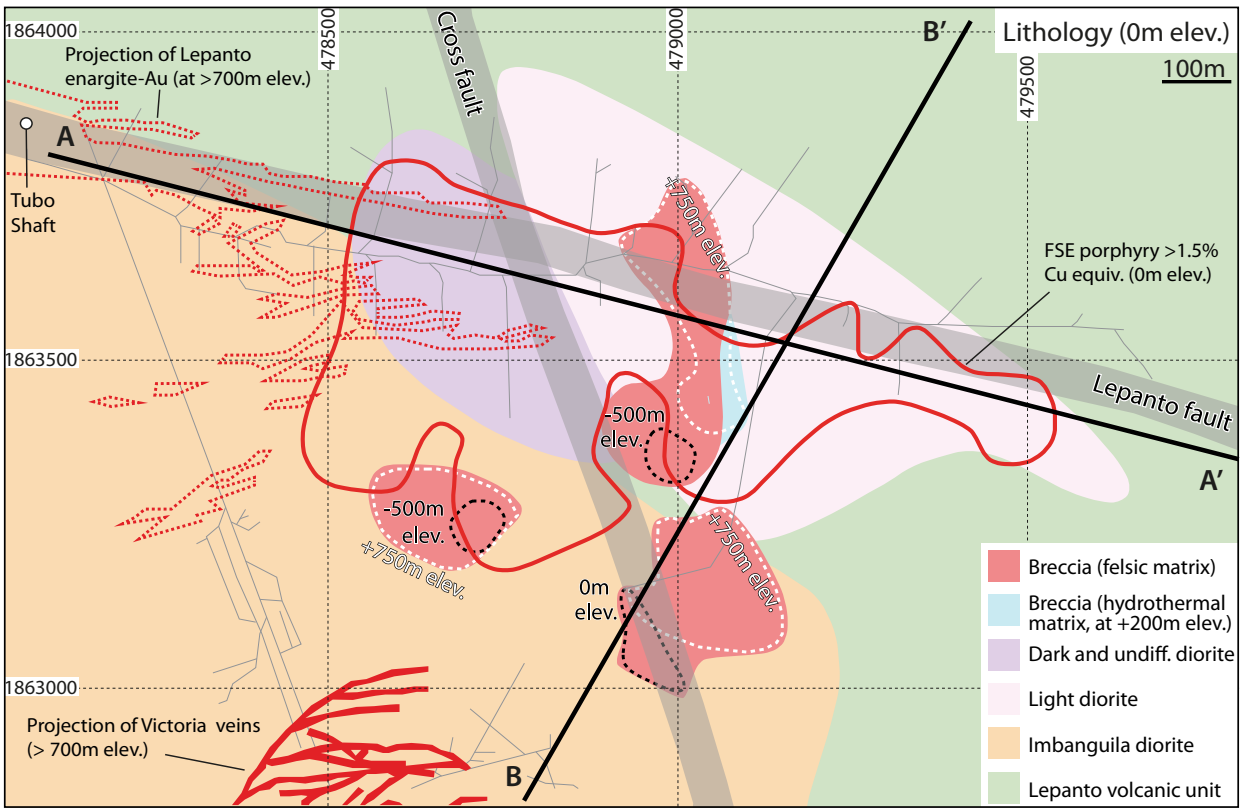

Fig. 2. Plan of lithology at 0-m elevation in the Far Southeast (FSE) porphyry copper system, showing the location of intrusions, fault zones, and the main ore envelope. The position of the breccia bodies (with either felsic or hydrothermal matrix) are plotted at different elevations, illustrating their pipe-like nature and the concentration of igneous and hydrothermal processes at Far Southeast. Underground workings (gray lines) are at 700-m elevation; A-A′ and B-B′ mark the locations of sections.

(n = 6), essentially the same as that of alunite within the overlying lithocap of 1.42 ± 0.08 Ma (n = 5; Arribas et al., 1995). Molybdenite from the Far Southeast deposit provided Re-Os dates of 1.50 ± 0.01 and 1.48 ± 0.01 Ma (Table 1; P. Dunkley, unpub. report, 2015). The subsequent overprint of white mica was dated with the K-Ar method; illite returned dates of 1.37 ± 0.05 to 1.22 ± 0.06 Ma (n = 10; Arribas et al., 1995).

Geology of the Far Southeast Deposit Below 700-m Elevation

The oldest and deepest host rocks intersected at Far Southeast are basaltic rocks of the Lepanto volcanic unit (Figs. 1B, 2). These were intruded by the Imbanguila diorite porphyry (Figs. 3A, 4), which was in turn intruded by the younger Far Southeast diorite intrusive complex. The complex is divided

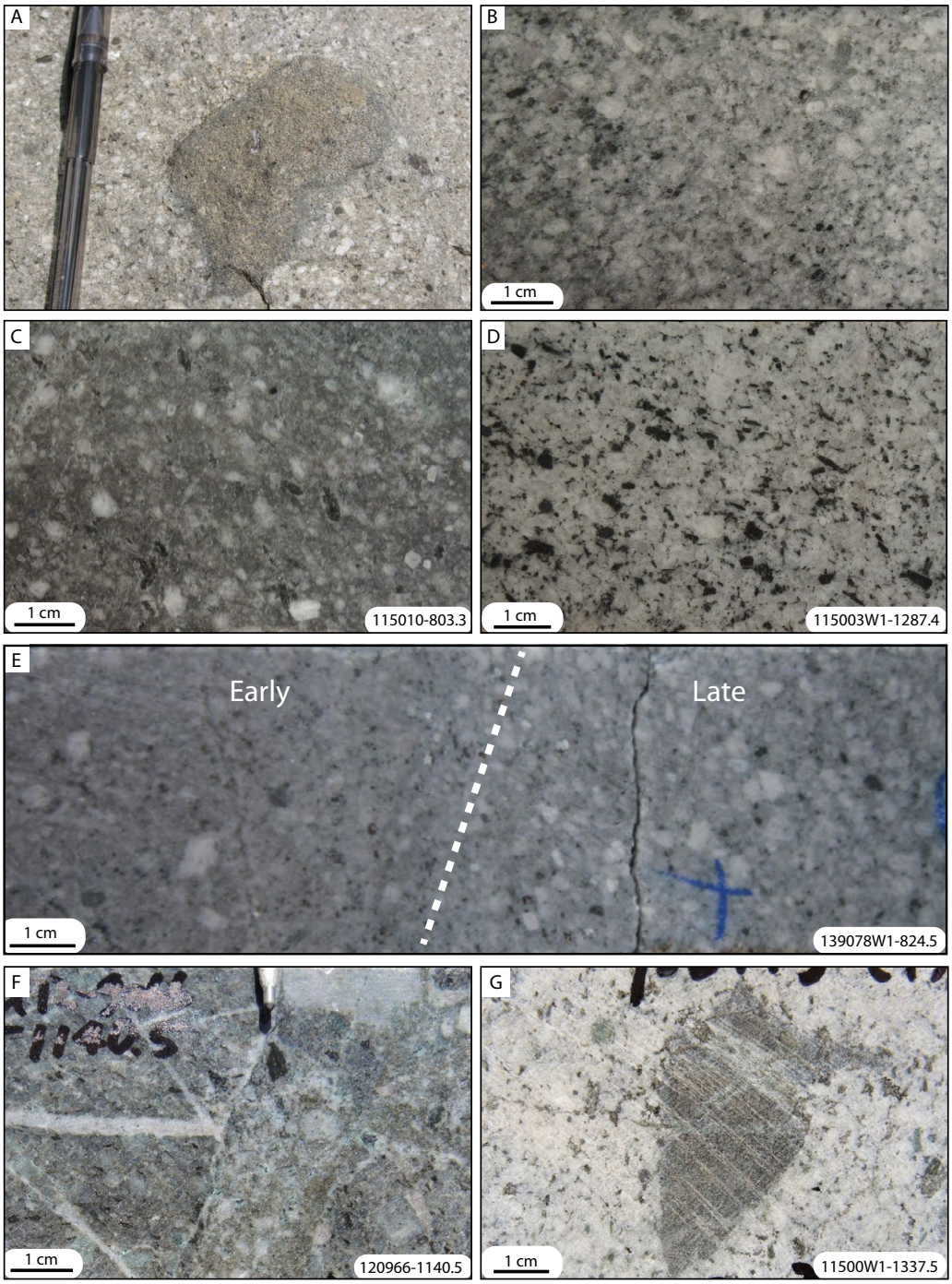

Fig. 3. Photographs of relatively unaltered lithologic units and crosscutting relationships (drill hole number and depth, in m, listed). A. Rounded mafic xenolith with chilled margins contained in Imbanguila porphyritic diorite. Surface locality: E479859 N1863245. B. Undifferentiated diorite. C. Porphyritic dark diorite. D. Equigranular light diorite. E. Later phenocryst-rich intrusion with chilled margin against an earlier phenocryst-poor intrusion. F. Truncated veins at intrusive contact. G. Light diorite with basalt clast containing veins truncated at margin; diorite also cut by later veins.

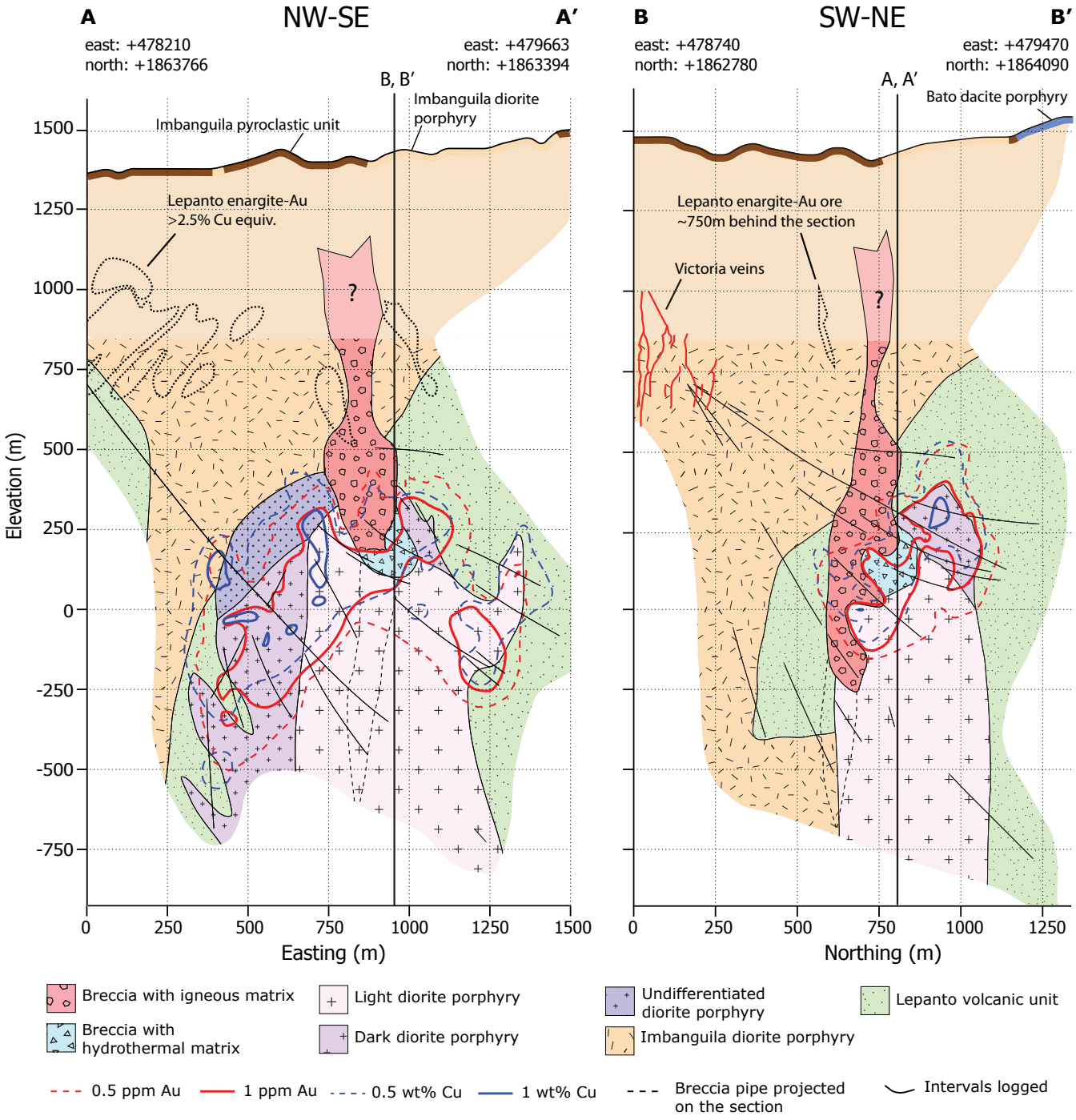

Fig. 4. Northwest-southeast and southwest-northeast sections (locations shown on Fig. 2) of lithology, with intrusions defined by features and crosscutting relationships on the basis of information from drill hole collars at 700- to –750-m elevation. Traces of logged drill holes shown for portions within ±100 m from each section. Copper (blue) and gold (red) shapes are shown for 1.0 and 0.5 wt % and 1.0 and 0.5 g/t, respectively. Visualization in three dimensions and creation of sections conducted with Leapfrog software.

into three diorite units by FSGRI workers (P. Dunkley, unpub. report, 2015), based on different granularity, color, groundmass/phenocryst ratios, and phenocryst mineralogy (quartz, plagioclase, hornblende). An early quartz diorite porphyry stock (Figs. 3B, 4), defined as undifferentiated diorite porphyry, is characterized by ~10% quartz, ~20% hornblende, and abundant plagioclase phenocrysts. This is cut by the dark diorite porphyry with less abundant quartz phenocrysts (<5%) and similar proportions of plagioclase and hornblende (Figs. 3C, 4). The youngest intrusion, the light diorite porphyry (locally equigranular), is characterized by <5% quartz, ~75% plagioclase, and ~20% hornblende phenocrysts (Figs. 3D, 4). The individual intrusive phases can be distinguished at their boundaries, locally with chilled margins (Fig. 3E), truncated

veins (Fig. 3F), or abrupt changes in quartz vein density. Most appear to be intermineralization in age, since xenoliths of the Lepanto volcanic unit with truncated quartz veins (Fig. 3G) are present. Away from the contacts, the intrusions are difficult to differentiate, particularly where altered, which posed a challenge to core logging and cross-section construction (Fig. 4). Some late-stage dikes are weakly altered by illite-chlorite but without veins.

The intrusive complex is cut by several breccia pipes (Figs. 2, 4). Within the drill hole intervals logged, two categories of breccia are recognized. One is a polymictic igneous breccia with a fine-grained igneous matrix, with clasts having blocky to wispy shapes and mostly porphyritic with andesite and dacite composition (Fig. 5A). Some clasts of diorite porphyry contain porphyry copper-style veins (Fig. 5B), some being fragments of quartz-magnetite veins (Fig. 5C), whereas other clasts are xenoliths of residual quartz with vuggy texture, derived from shallow lithocap levels or from an older lithocap at deeper position when this brecciation event occurred (Fig. 5D). These breccia bodies have a pipe shape with a slight angle from vertical and random azimuthal directions and widen upward, as shown in Figure 2. This type of breccia is interpreted to be of phreatomagmatic origin based on the wispy, likely juvenile clasts (Wright et al., 1980); the flaring-upward pipe shape is compatible with this hypothesis. The second breccia style is polymictic and clast supported (without apparent juvenile material); clasts have various alteration styles, some with clast-confined veins (Fig. 5E). The cement consists of hydrothermal quartz, anhydrite, chalcopyrite, and pyrite, leading to a hydrothermal breccia interpretation. The phreatomagmatic breccias cut through the diorite intrusions and/or the wall rock of Imbanguila and Lepanto volcanic unit and extend for an unknown distance above the intrusion complex (Figs. 2, 4). Some of the phreatomagmatic breccias are located just outside of the 1% Cu and 1 ppm Au ore shells. The hydrothermal breccia is hosted by the intrusion, adjacent to a magmatic breccia, and inside the 1% Cu and 1 ppm Au ore shell (Fig. 2).

Veins and Altered Rocks

Mineral assemblages (Table 2) were characterized by hand lens during core logging (e.g., Fig. 6) and SWIR analyses in the core shed, followed by laboratory study, including optical microscopy (Fig. 7), backscattered electron (BSE) imaging using a scanning electron microscope (SEM), and QEMSCAN examination of polished thin sections. Methodology is discussed further in the digital Appendix.

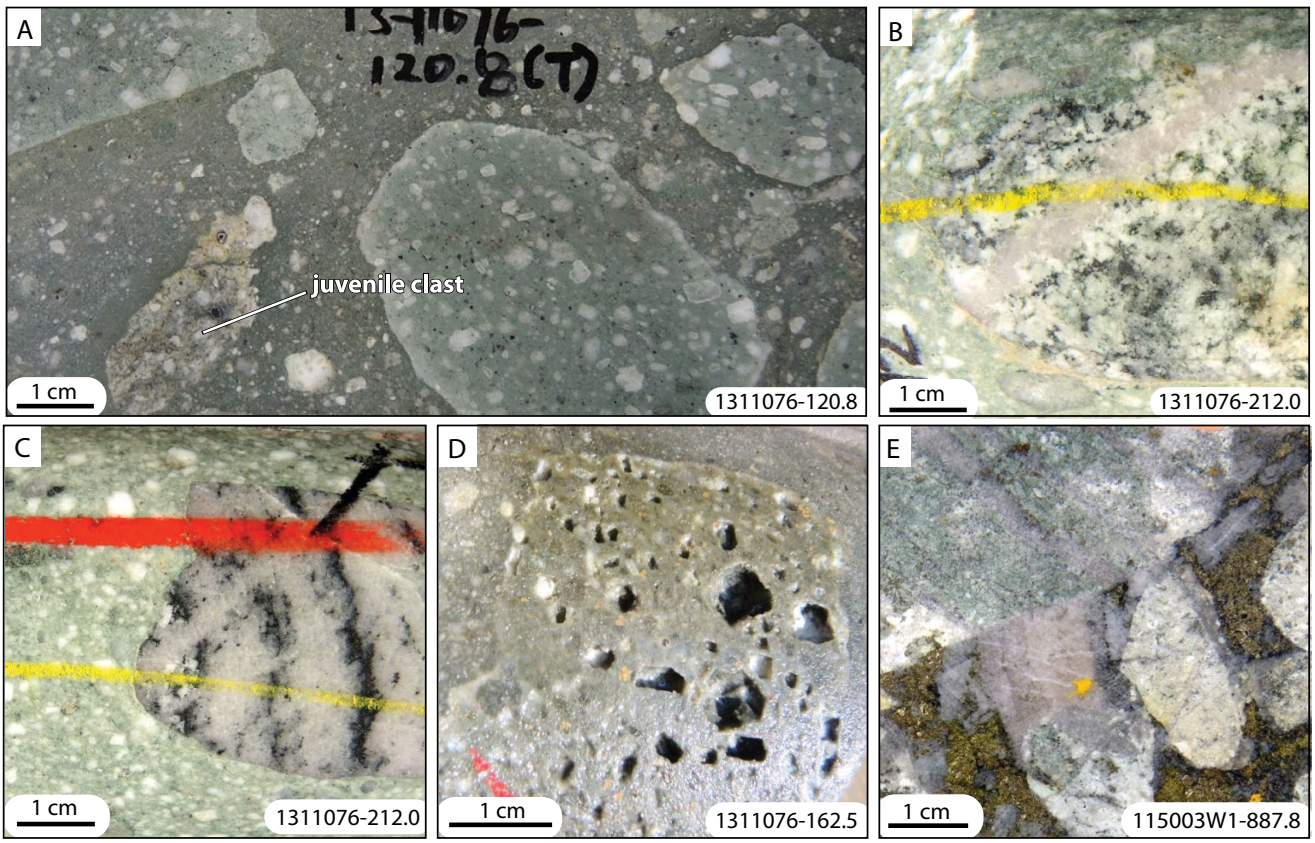

Fig. 5. Breccia bodies, both igneous and hydrothermal matrices (drill hole number and depth, in m, listed). Grade not determined for breccias with igneous matrix, but ~100 m below these samples, an average grade of 0.08 g/t Au and 0.03 wt % Cu was recorded over a 50-m interval. A. Matrix-supported polymictic phreatomagmatic breccia with juvenile clast, plus subangular to rounded porphyritic clasts. B. Undifferentiated diorite clast with veins in phreatomagmatic breccia. C. Clast of quartz-magnetite vein in phreatomagmatic breccia. D. Rounded clast of residual vuggy-textured quartz, reworked from lithocap level, in phreatomagmatic breccia. E. Clast-supported polymictic breccia with pyrite-rich hydrothermal matrix; clasts with strong white mica-chlorite-albite and white mica (greenish and bleached, respectively), many hosting truncated veins (0.80 g/t Au, 1.49 wt % Cu).

In the main porphyry deposit, a complex assemblage of veins and their alteration halos occurs. In places, vein alteration halos may be only a few millimeters wide. Halo widths increase with density of the related vein type, with halos around vein stockworks ultimately coalescing to form continuous alteration for tens to >100 m. Three stages of vein and alteration assemblages are recognized at Far Southeast: (1) veins of granular quartz-magnetite ± anhydrite ± biotite, with shreddy biotite + magnetite alteration halos, (2) veins of lavender to white quartz plus anhydrite and sulfides, with alteration halos of white-mica-chlorite-albite, and (3) sulfide-rich veins ± anhydrite ± quartz with bleached halos of white mica (Fig. 6). The spatial distribution of these assemblages is shown in Figure 8. Copper sulfides are observed in these three stages, within veins and alteration halos and disseminated in pervasive alteration. Pervasive propylitic alteration occurs outside the area of this study (Garcia, 1991).

There is also a veinlet-associated pervasive alteration of largely aluminosilicate minerals, locally with alunite, which occurs mostly above the top of the main porphyry deposit (above ~100- to 200-m elevation) up to ~700-m elevation (Fig. 8). At shallow depths (above ~700-m elevation, i.e., above the level of this study), a residual quartz-bearing part of the lithocap occurs at the unconformity between the Imbanguila and Balili or Lepanto volcanic unit. The residual quartz, locally with a vuggy texture, and a halo of quartz-alunite ± dickite and kaolinite, hosts the Lepanto high-sulfidation epithermal Au-Cu deposit (Garcia, 1991; Fig. 1B).

The locations of the 10 representative samples studied in detail with QEMSCAN are shown on the northwest-southeast section (Fig. 8). Sample information and the summary results are presented in Table 3. The results for five of these samples are presented here, with results from the other five samples included in Appendix Figures A1-A5.

Stage 1: Biotite-magnetite alteration halo to granular quartz veins

Stage 1 biotite alteration marks the earliest recognized hydrothermal event, as evidenced by crosscutting relationships of veins (Fig. 6A). Veins are typically wavy in appearance (Fig. 6A, B) and characterized by granular quartz with common magnetite, local anhydrite, and coarse-grained biotite (Fig. 6B, C). Most are dominated by quartz, but hairline magnetite-rich veins also occur. Biotite crystals (<100 µm in size) with a shreddy texture and magnetite occur scattered throughout the groundmass of the intrusions (Fig. 7A) and surrounding Lepanto volcanic unit and within granular quartz veins (Fig. 7B). Copper sulfides are typically not abundant, but bornite has been attributed to this stage. This alteration style is not closely associated with the high-grade Cu-Au zone.

Stage 1 is principally preserved below –250-m elevation, just below the 1 ppm Au grade shell and ~100 m below the 0.5 wt % Cu grade shell in drill holes on the northwest-southeast section (Fig. 8). This style of alteration mostly occurs within intrusions but has been observed up to 250 m into the Lepanto volcanic unit. It is locally preserved at shallower levels

Table 2. Summary of the Main Hydrothermal Alteration Styles at the Far Southeast Porphyry Deposit, Listed in Paragenetic Order

Simplified alteration stages	Depth range	Timing with respect to porphyry mineralization	Wall-rock alteration mineral assemblage	Hydrothermal veins	Sulfides in veins
Advanced argillic (AA) Lithocap	~700–1,300 m a.s.l.	Pre-ore (syn-biotite)	Residual quartz-halos of quartz-alunite-kandite ± pyrophyllite ± diaspore	Late quartz	Enargite-luzonite-covellite ± Au
Advanced argillic (AA) Aluminosilicate	~100–700 m a.s.l.	Overlaps with late syn-ore porphyry as well as syn-lithocap-hosted epithermal ore	Pyrophyllite-diaspore-kandite-quartz-anhydrite-illite ± alunite ± woodhouseite ± andalusite ± dumortierite	Anhydrite-quartz-hematite ± barite ± diaspore ± woodhouseite	Pyrite-chalcopyrite ± bornite ± chalcocite ± covelite ± digenite ± sphalerite ± molybdenite ± enargite ± luzonite
Stage 3 White mica	~-750–500 m a.s.l.	Syn- to late syn-ore	White mica-quartz-anhydrite-hematite-pyrite ± bornite ± apatite ± chalcopyrite ± tourmaline	Anhydrite-quartz-white mica ± hematite ± sheelite ± apatite ± goethite	Pyrite-chalcopyrite ± tennantite
				Paint veins ± anhydrite ± quartz[1]	Chalcopyrite-bornite
Stage 2 White mica-chlorite-albite	~-500–500 m a.s.l.	Syn-ore	Greenish white mica-albite-chlorite-quartz-anhydrite-hematite-magnetite-pyrite-chalcopyrite ± sphene ± rutile ± tourmaline	Euhedral lavender quartz-anhydrite ± hematite ± magnetite ± epidote	Chalcopyrite-pyrite ± bornite ± covellite ± chalcocite ± digenite ± molybdenite ± Au
Stage 1 Biotite	Below -750–500 m a.s.l.	Pre- to early syn-ore	Quartz-biotite-magnetite-K-feldspar-anhydrite ± epidote ± fluorite	Granular white/gray quartz-biotite-anhydrite-magnetite ± hematite ± epidote	± Bornite ± chalopyrite
				Magnetite ± hematite	NA

Note: Mineral positions reflect abundance; the lithocap alteration that hosts the Lepanto high-sulfidation epithermal deposit (Claveria, 2001; Chang et al., 2011) above 700-m elevation was not examined in this study; stages should not be viewed as sharp in time and space, but gradational; fluid pulses and fluctuation of fluid conditions are indicated by seemingly contradictory evidence

m a.s.l. = m above sea level

[1]With or without white-mica halo

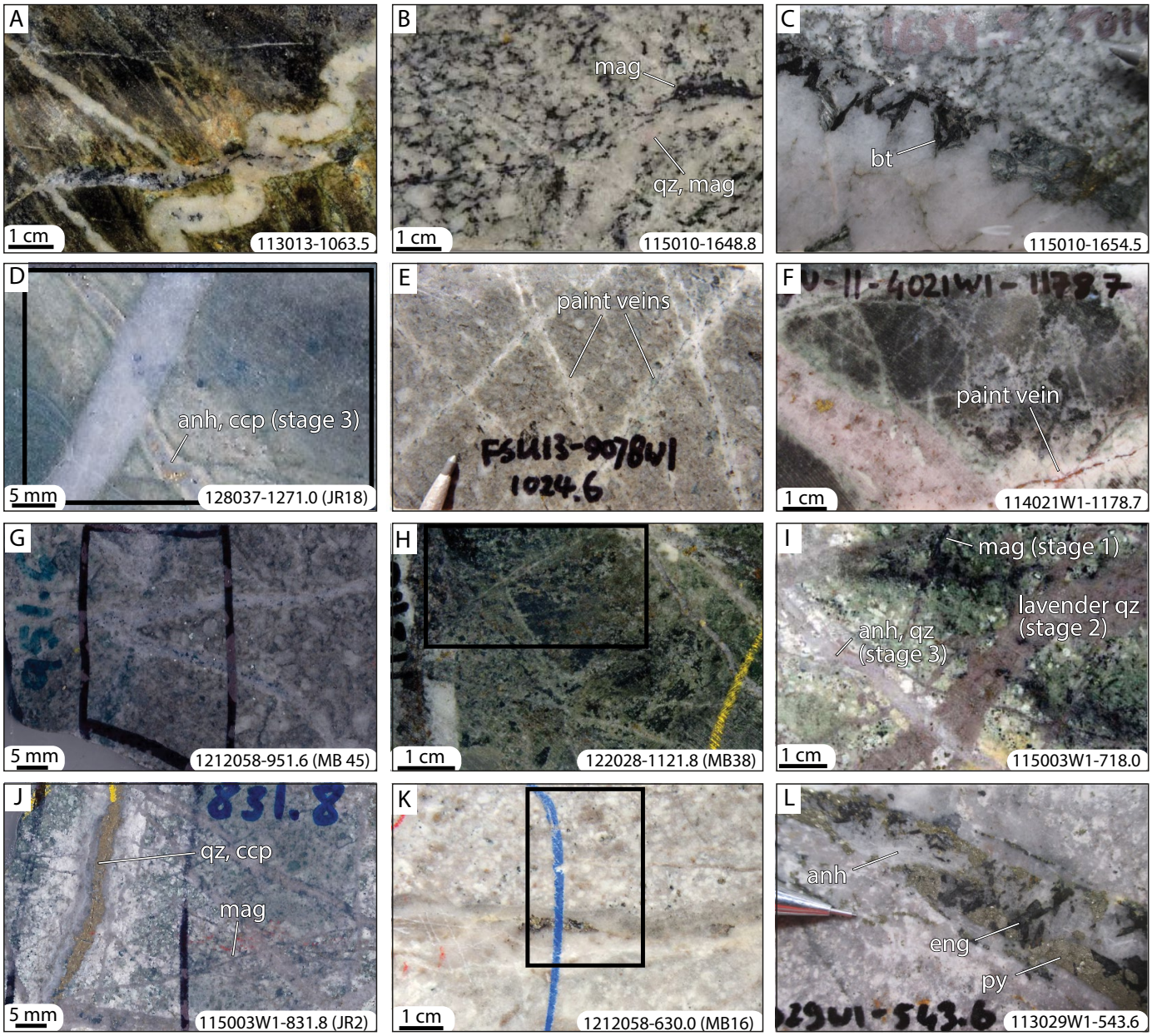

Fig. 6. Slabs of drill core (drill hole number and depth, in m, listed), with D, G, H, J, and K also examined by QEMSCAN in the area outlined in black. A. Undulated quartz vein with magnetite centerline cut by quartz-magnetite-chalcopyrite vein in biotite-altered Lepanto volcanic unit (0.77 g/t Au, 0.53 wt % Cu). B. Wavy magnetite-rich vein in biotite-altered light diorite (0.05 g/t Au, 0.09 wt % Cu). C. White, granular quartz and biotite vein in biotite-altered light diorite (0.04 g/t Au, 0.05 wt % Cu). D. White, granular quartz-anhydrite vein and an anhydrite-chalcopyrite vein with a white-mica halo (0.45 g/t Au, 0.39 wt % Cu). E. Chalcopyrite and bornite paint veins in white-mica–chlorite-albite–altered dark diorite (0.60 g/t Au, 0.75 wt % Cu). F. Lavender quartz-chalcopyrite with white-mica–chlorite-albite halo crosscut by thin Cu sulfide vein with white-mica halo (0.83 g/t Au, 0.36 wt % Cu). G. Quartz, anhydrite, and bornite veins in biotite and chlorite-altered dark diorite (1.77 g/t Au, 1.02 wt % Cu). H. Anhydrite, quartz, and chalcopyrite fractures in white-mica–chlorite-albite–altered Lepanto volcanic unit (0.37 g/t Au, 0.49 wt % Cu). I. Multiple magnetite veins cut by lavender quartz vein, cut by anhydrite and quartz vein with white-mica halo in white-mica–chlorite-albite–altered undifferentiated diorite (0.71 g/t Au, 0.76 wt % Cu). J. White-mica–chlorite-albite–altered light diorite crosscut by a quartz, anhydrite, and chalcopyrite vein with a white-mica alteration halo (4.62 g/t Au, 1.74 wt % Cu). K. Quartz, anhydrite, and Cu sulfide vein in white mica, anhydrite, pyrophyllite, and diaspore-altered Imbanguila diorite (0.64 g/t Au, 0.51 wt % Cu). L. Anhydrite, pyrite, and enargite vein in aluminosilicate-altered Imbanguila diorite (0.25 g/t Au, 0.32 wt % Cu). Abbreviations: anh = anhydrite, bt = biotite, ccp = chalcopyrite, eng = enargite, mag = magnetite, py = pyrite, qz = quartz.

Table 3. Samples Analyzed by QEMSCAN, Ordered by Decreasing Elevation (discussed in text and Appendix)

Sample ID	Thin section no.	Figure no.	Host lithology	Easting (m)	Elevation (m a.s.l.)	Core sample grade: Au (ppm)	Core sample grade: Cu (%)	Dominant alteration and temporal sequence: Bt	WCA	White mica	Alumino-silicate	Description
1212058-630.1	MB16	Fig. 13	Imbanguila diorite	375	200	0.6	0.5			(•)	•	Qz vein reopened by anh, py in white-mica alteration with incipient prl and dsp crystallization
1311076-1076.5	MB51	App. Fig. A3	Lepanto volcanic unit	1110	170	1.2	0.9			•		Numerous qz, anh, ccp veins in strongly silicified and white-mica–altered host rock
122028-1121.8	MB38	Fig. 9A	Lepanto volcanic unit	1230	160	0.4	0.5	• →	•			Anh, ccp fractures with ab halo and qz vein in white mica, chl–altered rock
115003W1-831.8	JR2	App. Fig. A4	FSE complex (light diorite)	725	120	4.6	1.8		• →	•		Ccp, anh, qz vein with qz, white-mica halo in ab, chl, ms–altered rock
139078W1-900.9	MB57	App. Fig. A5	FSE complex (dark diorite)	600	100	2.0	1.6		• →	•		Qz, anh, ccp, veins in ab-rich, chl, white mica (top) and white-mica (bottom)–altered rock
139078-1026.9	JR22	App. Fig. A1	FSE complex (dark diorite)	570	30	1.1	0.7	• →	•			Qz, anh, ccp, bn vein with associated pervasive ab, white mica, anh, chl alteration overprinting earlier kfs, anh alteration of primary plagioclase
1212058-951.6	MB45	Fig. 9B	FSE complex (dark diorite)	600	-50	1.8	1.0	• →	•			Qz, anh, bn veins with associated pervasive ab, chl, Fe oxide, anh alteration overprinting earlier kfs, anh, bt alteration of primary igneous assemblage
1212058W1-964.5	MB18	App. Fig. A2	FSE complex (dark diorite)	615	-60	1.9	1.0	• →	• →	•		Qz, anh, ccp vein with white-mica halo and qz, anh, ccp vein with pervasive ab, white mica, chl alteration overprinting earlier kfs, anh alteration
115010-1301.8	JR5	Fig. 9C	FSE complex (light diorite)	805	-375	0.2	0.1	• →	• →	•		Py, anh, qz, vein with halo of white mica, anh replacing primary phenocysts in ab, chl–altered rock
128037-1271.0	JR18	Fig. 9D	Lepanto volcanic unit	380	-415	0.5	0.4	• →	• →	•		Qz, anh vein crosscut by anh, ccp, qz vein with white mica, chl halo in white mica, chl, ab–altered rock overprinting earlier kfs, anh alteration

Notes: Copper and gold grades listed are for the 2.5-m core interval that included the sample; arrows signify overprinting, and parentheses and line signify that the overprinting is assumed
Abbreviations: ab = albite, anh = anhydrite, bn = bornite, bt = biotite, ccp = chalcopyrite, chl = chlorite, dsp = diaspore, FSE = Far Southeast, kfs = K-feldspar, m a.s.l. = m above sea level, ms = muscovite, prl = pyrophyllite, py = pyrite, qz = quartz, WCA = white mica-chlorite-albite

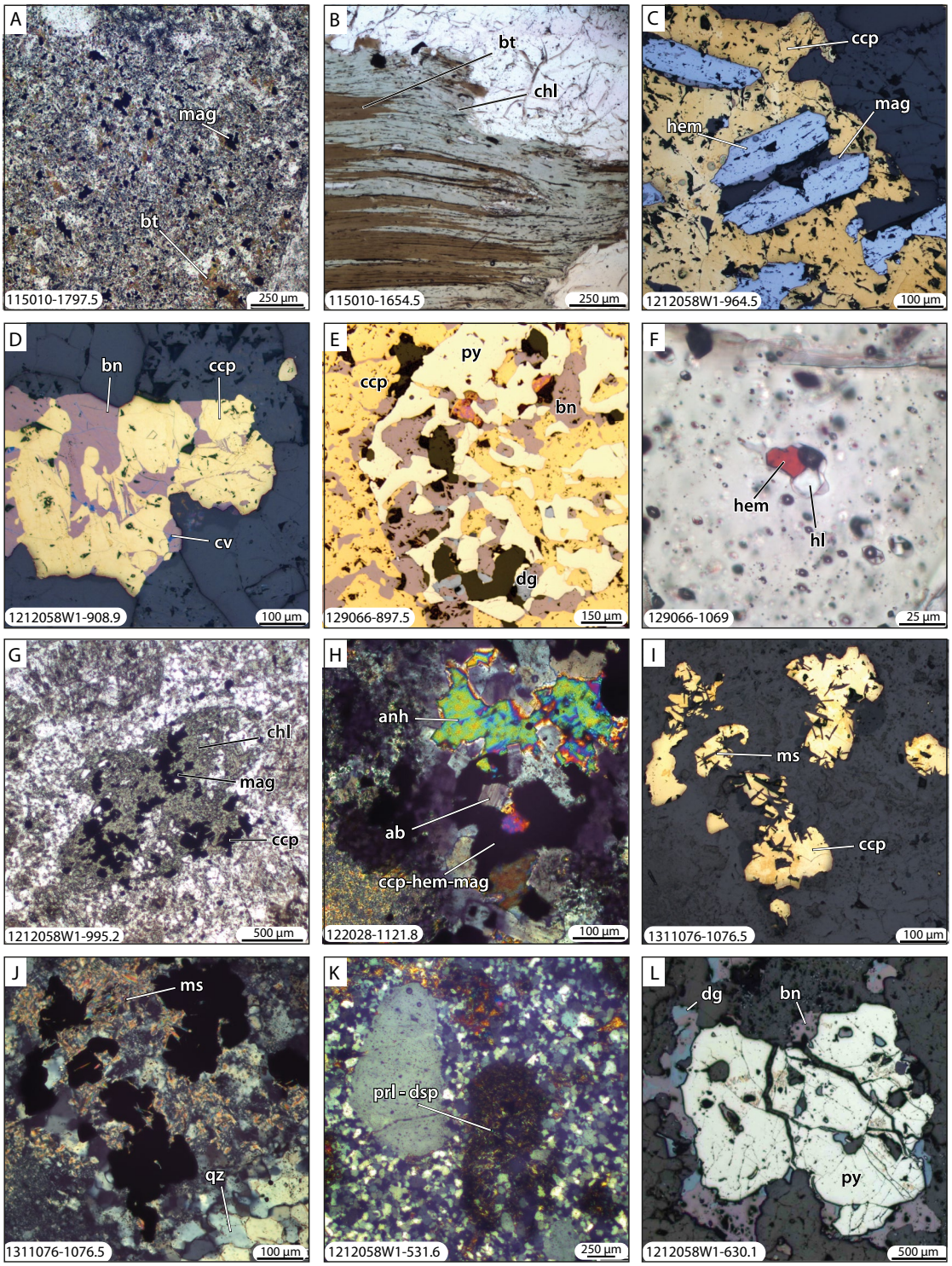

Fig. 7. Photomicrographs of key hydrothermal features. A. Magnetite and biotite in pervasive biotite alteration (transmitted light). B. Chlorite replacing biotite in vein associated with biotite alteration (transmitted light). C. Fe oxide relationship of magnetite and hematite, associated with chalcopyrite (reflected light). D. Chalcopyrite, bornite, covellite within quartz vein (reflected light). E. Swiss cheese texture of pyrite replaced by chalcopyrite, bornite, and digenite (Bunce, 2015; reflected light). F. Large hematite daughter mineral in fluid inclusion in lavender quartz (transmitted light). G. Mafic crystal (hornblende) replaced by chlorite, magnetite, chalcopyrite (transmitted light). H. Albite crystal associated with minerals of hydrothermal origin in white-mica–chlorite-albite alteration (transmitted light). I. Chalcopyrite with bladed white-mica intergrown with sulfide (reflected light) and J. (transmitted light). K. Aluminosilicates and diaspore replacing felsic magmatic phenocryst (transmitted light). L. Pyrite, bornite, and digenite at 200-m elevation in aluminosilicate alteration (reflected light). Abbreviations: ab = albite, anh = anhydrite, bn = bornite, bt = biotite, ccp = chalcopyrite, chl = chlorite, cv = covellite, dg = digenite, dsp = diaspore, hem = hematite, hl = halite, mag = magnetite, ms = muscovite, prl = pyrophyllite, py = pyrite, qz = quartz.

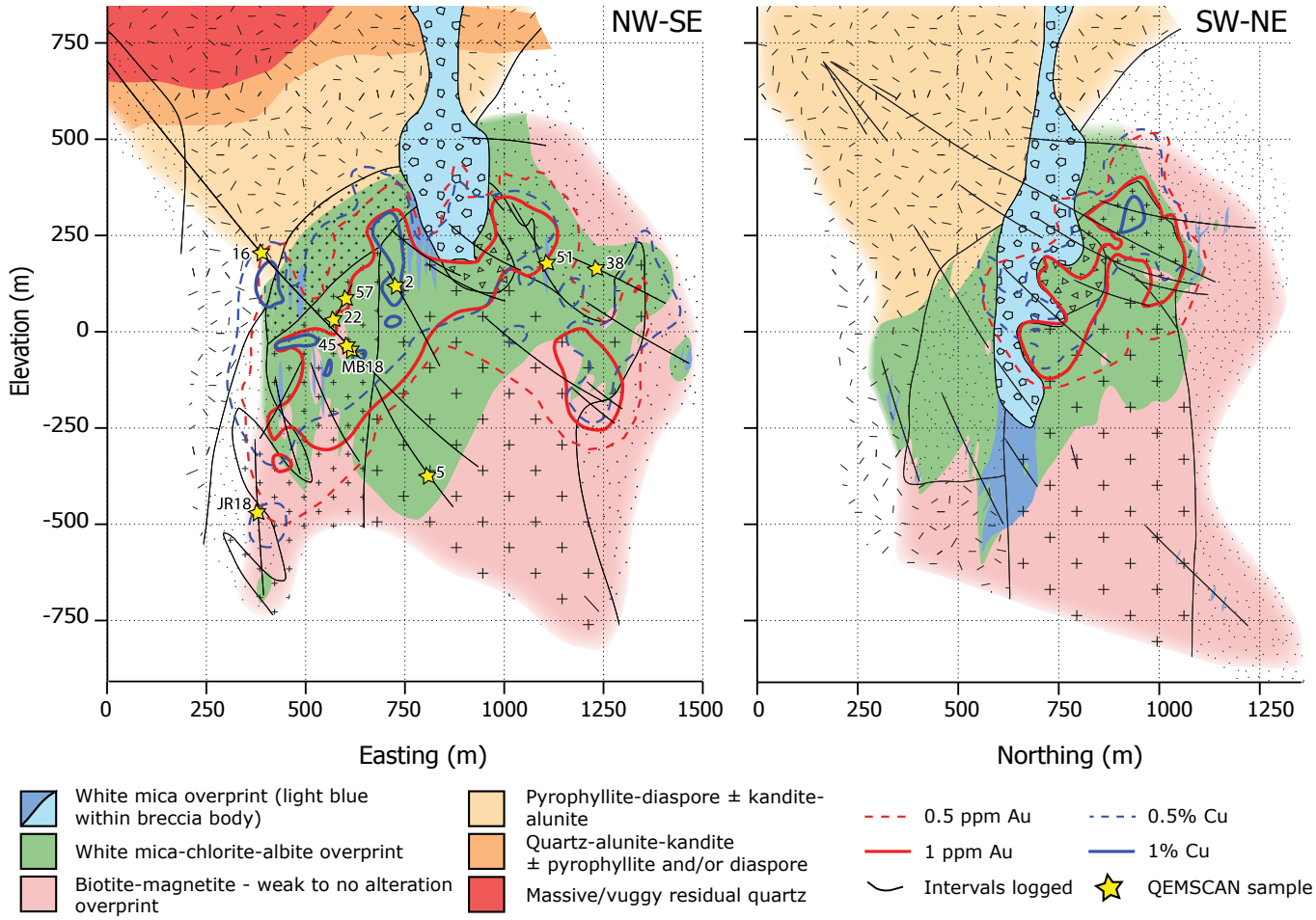

Fig. 8. Simplified spatial distribution of hydrothermal alteration associated with the Far Southeast porphyry copper deposit shown in two sections (lithology patterns are defined on Fig. 4). The existing Far Southeast Gold Resources, Inc. logging results of hydrothermal alteration from all 98 holes (102 km of core) were used to cross check the final model determined here based on our logging of 10.3 km of core. The locations of the samples analyzed by QEMSCAN are shown on the northwest-southeast section.

(up to 500-m elevation), mostly outside of the 0.5 g/t Au and 0.5 wt % Cu grade envelopes.

Stage 2: White-mica–chlorite-albite alteration associated with lavender quartz

Stage 2 veins are composed of euhedral lavender quartz, anhydrite, hematite plus minor magnetite, pyrite, and Cu sulfides (Fig. 6F). Hematite commonly replaces magnetite with the reverse locally observed (e.g., magnetite has locally replaced hematite as in Fig. 7C). In the high-grade zone, chalcopyrite is commonly replaced by bornite and later by covellite (Fig. 7D). The pyrite in the veins appears to be replaced by chalcopyrite and bornite, with a Swiss cheese texture, locally with incipient chalcocite and digenite replacement (Fig. 7E). Chlorite from stage 2 commonly replaces stage 1 hydrothermal biotite (Fig. 7B). The lavender color of these quartz veins may be caused in part by hematite daughter minerals in hypersaline fluid inclusions trapped in quartz crystals (Fig. 7F) coexisting with vapor-rich inclusions. As well as occurring in the rock matrix, this alteration replaced primary igneous minerals, so that hornblende has been replaced by chlorite, magnetite, and chalcopyrite (Fig. 7G). Copper sulfides also occur as thin (~1 mm) straight veinlets, referred to as paint veins, containing few or no other minerals (Fig. 6E).

Stage 2 veins have halos of white-mica–chlorite-albite wall-rock alteration. This is the dominant alteration type between 500- and –300-m elevation and is spatially associated with the high-grade copper and gold zone (Fig. 8). This alteration style has been observed in all lithologic units and occurs as narrow vein halos (Fig. 6F) but can become pervasive throughout the wall rock where stage 2 veins are abundant and halos coalesce (Fig. 6H). Late-mineralization breccias contain quartz diorite porphyry clasts affected by stage 2 alteration. Paint veins are typically hosted by stage 2 altered rock but can also have white-mica–rich alteration halos (Fig. 6F). Examination of stage 2 alteration by QEMSCAN (Fig. 9A) indicates that pervasive white mica and chlorite patches in distinct zones (0.5–2 mm in size), probably reflecting the original igneous texture and composition of the rock unit; white mica and chlorite likely replaced felsic and mafic minerals, respectively.

Gaibor et al. (2013) first recognized albite associated with the highest density of stockwork veins that coincide with the highest copper and gold grades. Hydrothermal albite can be

difficult to distinguish by optical microscopy alone due to its typical fine-grained and pseudomorphous character (as it maintains the original shape and optical features when igneous feldspars or groundmass are replaced). Typical hydrothermal albite (as blocky to tabular crystals, with characteristic parallel twinning) is coeval with anhydrite, magnetite, hematite, and chalcopyrite (Fig. 7H); the composition has been measured by microprobe (Fig. 10). The high albite content of stage 2 alteration (consisting of ~50% of sample MB45) is shown by QEMSCAN analyses to occur in two areas of study, 1 and 2 (Fig. 9B), more so in the former (73 and 43%, respectively, with plagioclase remaining in the latter).

The Al-OH absorption peak position of stage 2 white mica ranges from 2,188 to 2,225 nm, but is mostly >2,200 nm, with a mean of 2,203 nm (Fig. 11). The higher wavelength position indicates a higher Fe and Mg content (phengitic), accounting for the light-green color of the white mica (Uribe-Mogollon and Maher, 2018). The green color of stage 2 alteration (Fig. 6F, H, I) is likely caused by the dark-green chlorite plus light-green phengitic white mica. About 90% of illite crystallinity (IC) values of the white mica of this stage vary between 0.4 and 2.6 (App. Fig. A6), indicating that most of the white mica is illite to interlayered illite/smectite.

Stage 3: White-mica–quartz alteration associated with anhydrite-pyrite-quartz veins

Sulfide-rich (pyrite ± chalcopyrite)-quartz-anhydrite veins plus a white-mica alteration halo cut stage 1 and 2 assemblages (Fig. 6D, F, I, J). This assemblage occurs over a wide vertical range, from the deepest drill core (–750 m) up to ~500-m elevation, particularly associated with fractures within both the Lepanto volcanic unit and the Far Southeast diorite complex. White-mica alteration is also pervasive within and in part surrounding the vertical (pipe-like) breccia body with igneous matrix (Fig. 8), which formed relatively late, with lower metal grades. Stage 3 pyrite-anhydrite-quartz or anhydrite-chalcopyrite veins with a white-mica halo may cut and overprint the two previous stages, including white-mica–chlorite-albite (Fig. 9C) and biotite-magnetite–altered rock (Fig. 9D). There is also evidence for white-mica precipitation prior to or intergrown with chalcopyrite (Fig. 7I, J).

The Al-OH absorption peak position of stage 3 white mica ranges from 2,188 to 2,207 nm, mostly <2,198 nm, with a mean of 2,197 nm (Fig. 11B). Such lower wavelength positions typically indicate elevated Na content (paragonitic) and a low Fe-Mg content, which is consistent with the typical white color of the stage 3 white mica (Fig. 11A). Although the value ranges overlap, compared to stage 2 white mica, the Al-OH absorption feature of stage 3 white mica has a lower wavelength position (Fig. 11B).

A plot of white-mica composition (2,200-nm feature) of samples from all stages on the northwest-southeast and southwest-northeast sections (Fig. 12A) shows values of less than ~2,197 nm above ~300-m elevation on the southwest-northeast section. Both sections record values >2,203 nm within the high-grade zones (>1% Cu and >1 g/t Au), although there are high as well as low values outside the high-grade centers of the deposit. The lower white-mica wavelength features on both sections tend to correlate with the location of aluminosilicate minerals, particularly on the southwest-northeast section.

Fig. 9. Mineralogical analysis by QEMSCAN. A. Sample MB38 (drill hole 122028-1,121.8 m, 1230 mE, 160-m elevation), in Lepanto volcanic unit (0.37 g/t Au, 0.49 wt % Cu; Fig. 6H). Area within white outline enlarged in inset, along with plane-polarized light image; the QEMSCAN image (bottom) shows the intergrowth replacement of biotite by chlorite. Electron microprobe analyses of albite (yellow square) shown in Figure 10. B. Sample MB45 (drill hole 1212058-951.6 m, 600 mE, –50-m elevation), in dark diorite (1.78 g/t Au, 1.01 wt % Cu; Fig. 6G). Three quartz-anhydrite-bornite veins, with biotite and chlorite alteration in hand sample, biotite alteration overprinted by white-mica–chlorite-albite alteration. The Fe oxides were identified optically as magnetite. C. Sample JR5 (drill hole 115010-1,301.8 m, 805 mE, –375-m elevation), in light diorite unit (0.24 g/t Au, 0.07 wt % Cu). Pyrite, anhydrite, and quartz vein with a white-mica alteration halo in white-mica–chlorite-albite–altered light diorite. D. Sample JR18 (drill hole 128037-1,271.0 m, 380 mE, –415-m elevation), in Lepanto volcanic unit (0.45 g/t Au, 0.39 wt % Cu; Fig. 6D). E. Plane- and F. crossed-polar transmitted light of area of crosscutting veins (bottom of Fig. 9D). Detailed mineralogical observations: A. White-mica–chlorite-albite overprint of biotite-magnetite alteration. Pervasive white mica and chlorite patches in distinct zones (0.5–2 mm in size), likely replaced felsic and mafic minerals, respectively. Area 1 has 17% white mica, 33% quartz, and 16% chlorite, and area 2 has 39% white mica, 18% quartz, and 8.3% chlorite, reflecting alteration heterogeneity; both contain 27% albite and 1.1–1.3% chalcopyrite, respectively. Remnant biotite (1.5%) disseminated in section, along with ~1% Fe oxide. Vein types are (1) 5- to 50-µm-wide anhydrite-chalcopyrite paint veins with halos of albite and minor chlorite, cut by (2) quartz-rich veins with minor halos. Patch of anhydrite, quartz, and chalcopyrite with a halo of albite and minor chlorite grades outward to white mica (top); biotite partially replaced by chlorite with albite, anhydrite, quartz, and Fe oxide (hematite replacement of magnetite), inset. Microprobe spot analyses (located within the yellow box) confirms albite ($Or_1Ab_{96\text{-}98}An_{1\text{-}3}$; Fig. 10). B. Stage 1 biotite alteration with quartz-anhydrite-bornite veins overprinted by stage 2 white-mica–chlorite-albite alteration. Abundant albite in areas 1 and 2, more so in former (73 and 43%, respectively, with plagioclase remaining in the latter), typical of stage 2. Remnant biotite (1.7 and 5.3%) and magnetite is overprinted by chlorite (5.6 and 4.6%) and rutile. Bornite disseminated (1.3 and 0.06%) and also in quartz-anhydrite vein (replaced by chalcocite; see inset). C. Pyrite-anhydrite-quartz vein with white-mica halo cutting white-mica–chlorite-albite alteration. Stage 3 vein halo in area 1 contains 47% quartz, 45% white mica, 5% anhydrite, and 1% pyrite, plus minor chlorite, albite, and other minor minerals, possibly from prior alteration stages. Beyond the 6- to 9-mm-wide vein halo, mineralogy dominated by stage 2 alteration. D. White mica-chlorite-albite and white mica replacing biotite alteration. Deepest QEMSCAN sample; low grade for Far Southeast. 5-mm quartz-anhydrite vein plus minor chalcopyrite and ~1-mm-wide anhydrite-chalcopyrite vein with inner white-mica–rich halo and outer white-mica–chlorite-albite halo. Area 2 halo contains 45% white mica, 29% quartz, and 13% chlorite, with white mica, quartz, and minor chlorite in the immediate ~0.5 mm to vein. Area 1, pervasive white-mica–chlorite-albite halo to anhydrite-chalcopyrite vein; beyond halo, early biotite (6% remaining) overprinted by stage 2 alteration (14% albite, 18% chlorite, and 6% white mica). Thinner anhydrite-chalcopyrite vein with white-mica halo cuts thicker quartz-anhydrite vein, (Fig. 9E, F); quartz crystal directions modified in thicker vein. Ab = albite, An = anorthite, K-fsp = K-feldspar, Or = orthoclase.

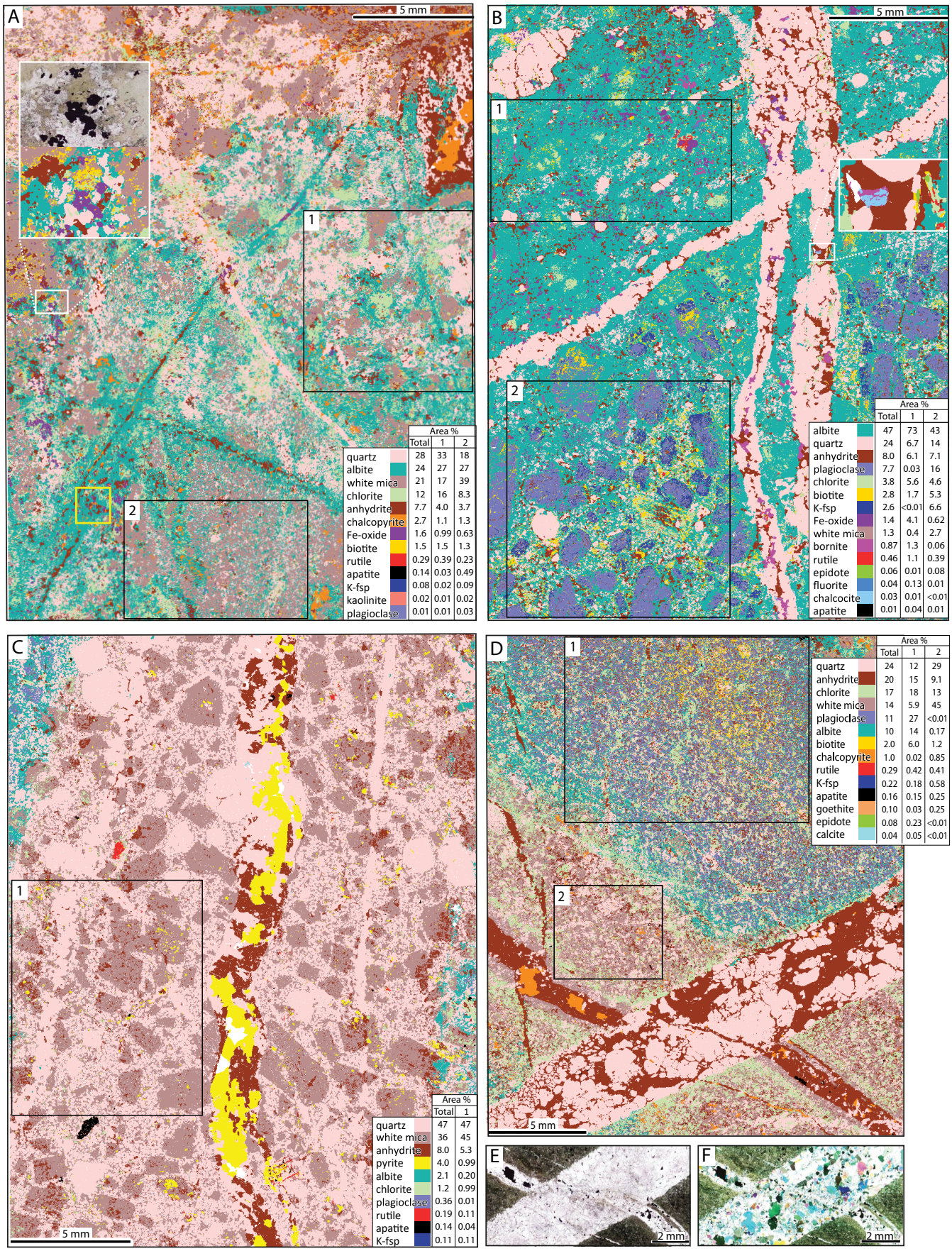

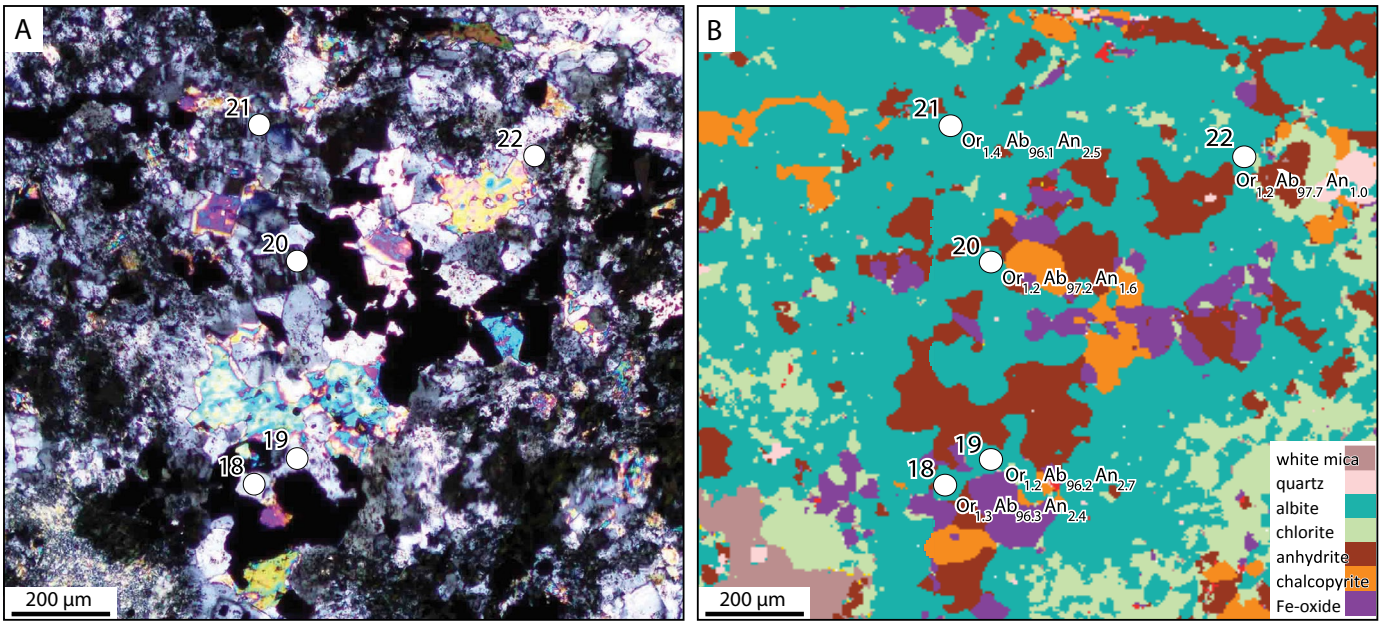

Fig. 10. Microprobe analyses. Data for each point in Appendix Table A2. A. Transmitted-light photomicrograph of sample 122028-1,121.8 m, MB38 (0.37 g/t Au, 0.49 wt % Cu). Albite and white mica with opaque minerals in groundmass (see Fig. 9A, yellow outline on QEMSCAN image). B. QEMSCAN results for area in A, with albite compositions from microprobe listed. Ab = albite, An = anorthite, Or = orthoclase.

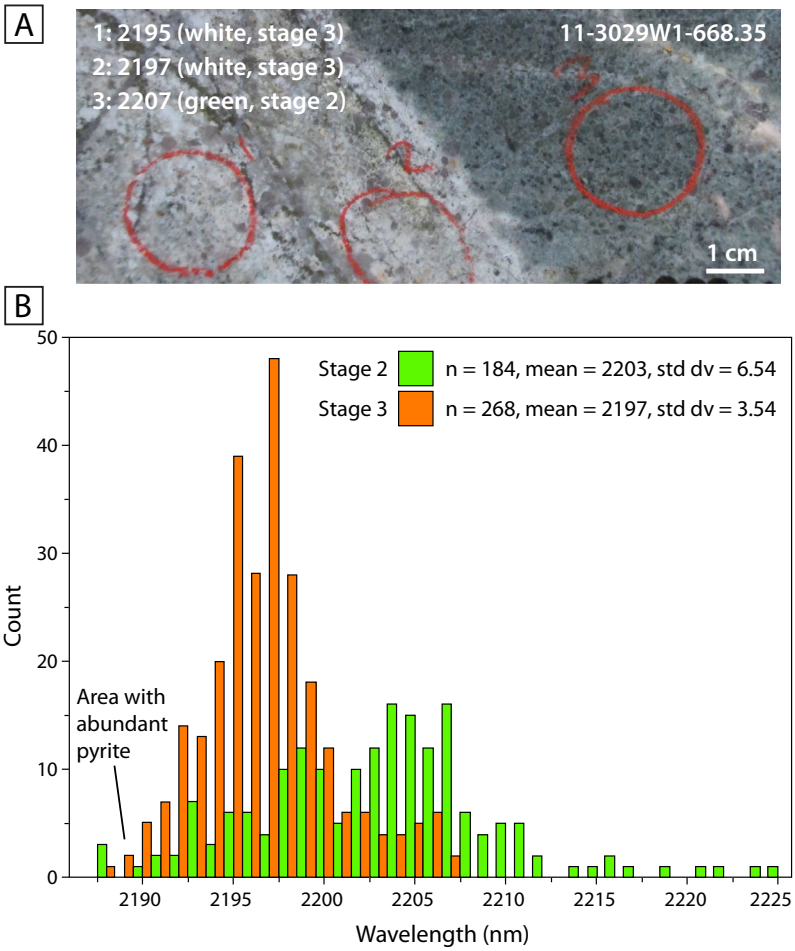

Fig. 11. A. Representative drill core showing sampling protocol for short-wave infrared (SWIR) analyses of altered samples containing white mica. The position of the nominally 2,200-nm peak of white mica is listed from the SWIR results (analyses within the three numbered red circles). Green and white note the alteration color. B. Frequency bar chart showing the number of core samples analyzed by SWIR (452 measurements from a total of 150 samples over ~10,300 m of core) vs. wavelength of the nominally 2,200 nm peak.

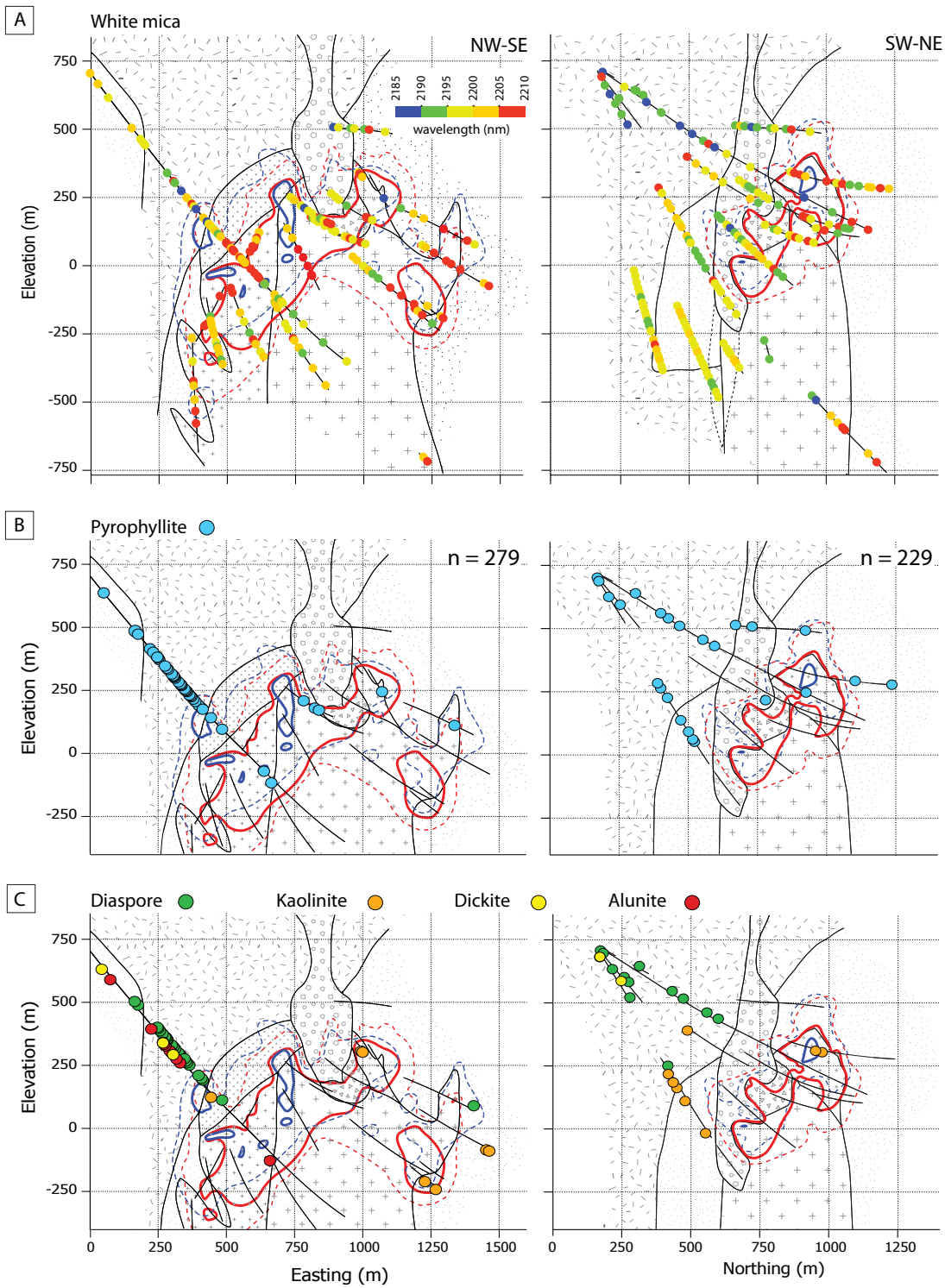

Fig. 12. A. Position of the nominal 2,200-nm white-mica peak for drill core samples analyzed by short-wave infrared (SWIR), plotted on northwest-southeast and southwest-northeast sections. White-mica peaks were recorded for pervasive alteration. B. Distribution of pyrophyllite and C. diaspore, alunite, and related aluminosilicate minerals based on SWIR analyses, in the transition between the lithocap base at ~700-m elevation to about sea level. Lithology patterns are seen on Figure 4.

Aluminosilicate alteration

At levels above the main porphyry orebody (mostly above 250-m elevation, within Imbanguila diorite porphyry), aluminosilicate alteration is pervasive, with variable assemblages that include pyrophyllite, diaspore, kandite, quartz, anhydrite, and/or illite, and minor to rare alunite, woodhouseite (an aluminum phosphate-sulfate mineral of the alunite group), andalusite, and dumortierite. Optical microscopy reveals

diaspore associated with aluminosilicate minerals in the rock matrix or replacing original feldspars (Fig. 7K). QEMSCAN analyses shows bleached and mottled pervasive alteration of quartz and white mica with pyrophyllite plus diaspore, cut by a quartz vein reopened by an anhydrite-rich vein with white mica, pyrite, bornite (replaced by chalcocite), barite, and woodhouseite (Fig. 13). The mineralogy of the aluminosilicate minerals was confirmed by SWIR spectroscopy (Fig. 12B, C); locally aluminosilicates were also identified at depth, along narrow structures. Aluminosilicate alteration is associated with veins of anhydrite-quartz ± hematite that variably contain pyrite, chalcopyrite, bornite, chalcocite, covellite, digenite, enargite, sphalerite, or molybdenite (Fig. 7L).

Discussion

Alteration types: Overprinting and evolution

The key characteristics of the various alteration and mineralization stages recognized at Far Southeast are summarized in Table 2. The main veins and their associated alteration minerals (Fig. 14) follow the general temporal sequence of early biotite (stage 1) to white-mica–chlorite-albite (stage 2) and then white mica (stage 3); at shallower depth, there is a transition from white mica to aluminosilicate alteration, up to the base of the earlier formed lithocap (during the biotite stage). Key minerals associated with these alteration types follow the long-recognized paragenetic sequence of biotite → chlorite → white mica → pyrophyllite, consistent with a sequence pre-

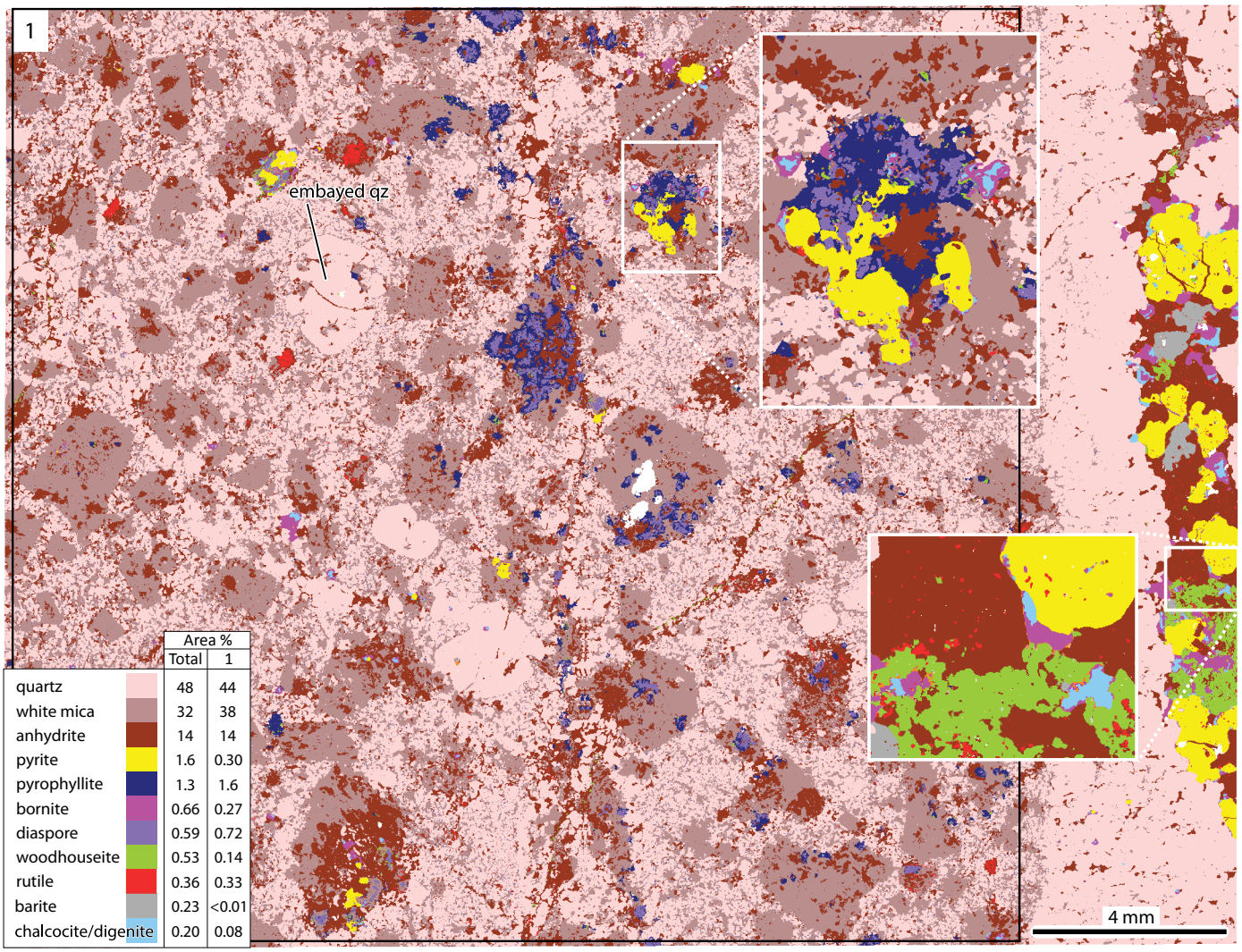

Fig. 13. Mineralogical (QEMSCAN) analysis of sample MB16 (drill hole 1212058-630.0 m, 375 mE, 200-m elevation), in Imbanguila diorite (0.64 g/t Au, 0.51 wt % Cu; Fig. 6K). Bleached and mottled pervasive aluminosilicate-altered rock with quartz vein reopened by anhydrite, pyrite, barite, and Cu sulfides. Within the inset (above), pyrophyllite, diaspore, and woodhouseite are intergrown with rutile, pyrite, and bornite (center exsolved to chalcocite/digenite), intergrown with white mica and anhydrite. Lower inset (right), late quartz vein with anhydrite, white mica, woodhouseite, pyrite, bornite (center replaced by chalcocite/digenite; light blue), and specks of rutile (between 5 and 50 μm in size), with barite along the vein; thin anhydrite vein with woodhouseite. Pervasive alteration 44% quartz, 38% white mica, 14% anhydrite, 1.6% pyrophyllite, and 0.7% diaspore, with patches of pyrophyllite and diaspore after white mica near anhydrite. Igneous quartz phenocrysts locally embayed. Qz = quartz.

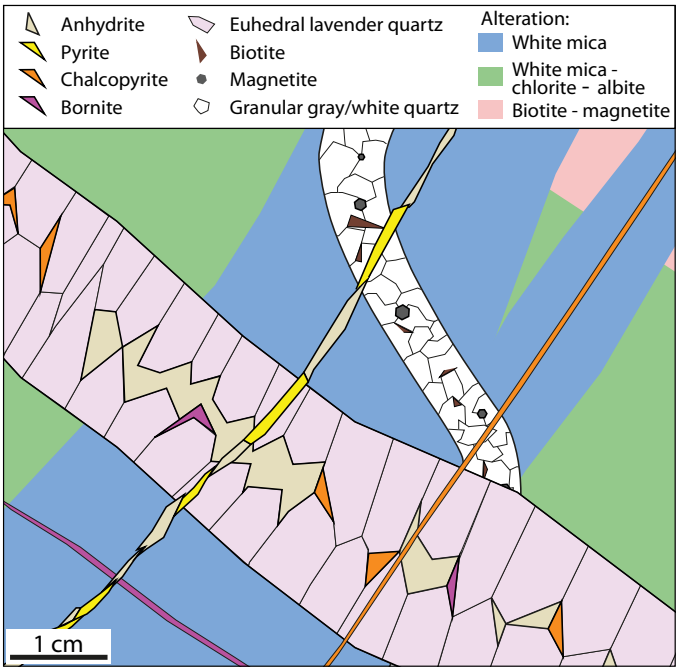

Fig. 14. Schematic representation of paragenetic relationships and mineralogy of major vein types, and associated alteration styles. Crosscutting relationships indicate timing, from earliest stage 1 ductile quartz vein (associated with biotite-magnetite alteration) followed by stage 2 euhedral lavender quartz vein (associated with white-mica–chlorite-albite alteration) and to stage 3 sulfide-rich paint vein (associated with white-mica–chlorite-albite alteration and white-mica-only halo) and pyrite-anhydrite vein (associated with white-mica-only halo).

dicted by a decrease in temperature as well as an evolution in fluid composition (Hemley and Jones, 1964; Hemley et al., 1980; Seedorff et al., 2005; Sillitoe, 2010).

At depth (below –250-m elevation), early biotite represents the highest temperature alteration (500°–550°C; Hedenquist et al., 1998); K-feldspar (Fig. 9B), and magnetite, commonly replaced by hematite, is also present. This high temperature is consistent with the sinuous nature of the associated quartz veins (Fig. 6A, B), indicating a plastic rheology of the rock (Gustafson and Hunt, 1975). Subsequently, biotite is widely replaced by chlorite (Fig. 7B), interpreted to be due to system cooling (Seedorff et al., 2005). Early sulfides associated with the biotite stage are dominated by bornite, as well as digenite and covellite, whereas chalcopyrite dominates stage 2.

A large amount of albite is associated with stage 2 alteration, up to ~40–70% of the rock, as quantified by QEMSCAN (Fig. 9B), indicating Na mobility during this period of alteration. In stage 2 alteration, albite follows anhydrite, as seen in thin fractures (Fig. 9A) and within the rock matrix (Fig. 9B; App. Figs. A1, A2, A5). Compositional analyses of hydrothermal plagioclase associated with stage 2 alteration confirms the presence of albite ($Or_1Ab_{96–98}An_{1–3}$; Ab = albite, An = anorthite, Or = orthoclase; Fig. 10). This alteration style identified at Far Southeast (Gaibor et al., 2013) is partly analogous to the sericite-clay (illite)-chlorite alteration first noted in Philippine porphyry copper deposits (previously referred to as SCC; Sillitoe and Gappe, 1984). Thus, it is possible that other deposits with previously identified chlorite-sericite alteration (Sillitoe, 2010) may also contain significant but unrecognized albite, due to its fine grain size and tendency to replace and retain the shape of igneous minerals.

Stage 2 alteration style is overprinted by white-mica alteration, which typically occurs as halos to straight anhydrite and pyrite-rich quartz veins (Fig. 9C). This hydrothermal event represents the waning period of the mineralizing system. The SWIR Al-OH wavelength of the white mica decreases from white-mica–chlorite-albite to white-mica-only alteration (Fig. 11), caused by a trend from more Fe-Mg–rich toward more K-Na–rich illitic minerals.

The IC determined by SWIR correlates with IC determined from X-ray diffraction (XRD) (Doublier et al., 2010), which is known to be related to formation temperatures (e.g., Frey, 1987). Based on our experience, SWIR-IC values >3.5 are typically obtained from coarse-grained muscovite associated with porphyry, greisen, and pegmatite deposits, which may form at >350°C. By contrast, IC values <0.5 are typically smectite that forms at temperatures of ~150°C (Hedenquist and Arribas, 2022). Most IC values at Far Southeast are between 0.8 and 2.5 (App. Fig. A6). Samples from a shallow depth, with IC values of 0.8–1.5, are from an area on the porphyry margin. Nearby, a fluid inclusion assemblage in quartz with white mica—suspected to be illite—returned a value of 280°C from the edge of the high-grade zone (Hedenquist et al., 1998).

Aluminosilicate alteration occurs mainly at ~700 m to as deep as ~100- to 200-m elevation (Fig. 8), including pyrophyllite, diaspore, and kandite minerals along with minor alunite. This alteration is typically present with quartz-anhydrite veinlets that contain pyrophyllite, diaspore, and woodhouseite, which cut white-mica alteration (Fig. 13), consistent with cooling from white-mica conditions (Hemley et al., 1980; Watanabe and Hedenquist, 2001). The sulfide assemblage (pyrite-bornite-chalcocite; Figs. 7L, 13) indicates a high-sulfidation state, consistent with the mineralogy of the overlying lithocap-hosted enargite-luzonite-gold (telluride) deposit (Gonzalez, 1959; Claveria, 2001). Cooling of fluid originally in equilibrium with white mica continued through the aluminosilicate zone and into the residual quartz lithocap that hosts the Lepanto high-sulfidation deposit, with cooling—in an environment of limited rock buffer capacity—again being the main cause of the shift from intermediate- to high-sulfidation-state sulfides (Einaudi et al., 2003). This ascent of deep liquid contrasts with the earlier vapor condensates that initially formed the barren residual quartz lithocap and quartz-alunite alteration halo (Hedenquist et al., 1998). Distinguishing the features of both styles (i.e., formation environments) of advanced argillic alteration (shallow lithocap due to vapor condensation vs. deeper aluminosilicate cooled from white mica) is essential to better understand their position relative to a potential porphyry deposit (Hedenquist and Arribas, 2022).

Criteria for the timing of this aluminosilicate ± minor alunite alteration type are not straightforward. There is a partial overlap of the mineralogy of this style with that of the lithocap, including kandite and alunite plus pyrophyllite. Macroscopically, this assemblage is observed to cut and overprint white-mica–chlorite-albite alteration, consistent with it being contemporaneous with (but shallower than) most white-mica

alteration, which distinguishes it from the early formed and shallow lithocap alteration. This distinction is also supported by isotopic analyses of the pyrophyllite (Hedenquist et al., 1998), with pyrophyllite and white mica sharing a similar formational fluid of largely magmatic origin, indicating that the aluminosilicate-dominated alteration is the shallow equivalent of stage 3 white mica.

Alteration mineralogy and grade distribution

Information from drill core logging, along with SWIR analyses to help clarify mineralogy, and copper and gold grades are plotted on lithology cross sections (Fig. 8), encompassing a volume of ~2.5 km^3. The higher copper and gold grades tend to overlap, as is typical of porphyry Cu-Au deposits worldwide (Esperanza, northern Chile, Perelló et al., 2004; Pebble, Alaska, Gregory et al., 2013; Grasberg, Indonesia, Leys et al., 2019), and are located at the top of the Far Southeast diorite complex (between an elevation of about –300 and 500 m), confirming the relationship between the three observed intrusions and metal distribution. High grades of copper and gold (>1% Cu and 1 g/t Au) are most closely associated with intense white-mica–chlorite-albite alteration, whereas biotite alteration is associated with grades that are typically ≤0.5 g/t Au and ≤0.5 wt % Cu (Fig. 8).

As determined from detailed logging by company geologists, an approximate estimate of copper deposition at Far Southeast is about 30% associated with the biotite stage, 50% in the high-grade white-mica–chlorite-albite stage, and perhaps 20% in the white-mica stage. Most Cu sulfides are associated with postbiotite alteration, but they have, nonetheless, been observed in multiple alteration stages. This, along with observed contradicting paragenetic relationships, is testament to fluid pulses and fluctuations of fluid conditions, similar to that modeled by Weis et al. (2012). Major and high-grade metal (copper and gold) deposition (Gaibor et al., 2013) was associated with lavender quartz-anhydrite veins and related white-mica–chlorite-albite alteration, as well as chalcopyrite or bornite paint veins (Fig. 6E, F; with or without a white-mica alteration halo).

Stage 2 alteration was overprinted by white-mica alteration and the aluminosilicate style (pyrophyllite, diaspore, dickite) at shallower levels as the system cooled to <300°C, the temperature limit deduced for this assemblage (Hemley et al., 1980; Watanabe and Hedenquist, 2001). Both white-mica-only and aluminosilicate styles of alteration tend to be associated with lower grades (perhaps due to remobilization of earlier deposited metals), although halos containing these alteration assemblages can occur adjacent to quartz-chalcopyrite veins and high-grade intervals (white-mica halos, App. Figs. A3, A4, and aluminosilicate veins, Fig. 13). This period was also contemporaneous with the emplacement of the breccias, possibly triggered by the intrusion of even deeper diorite bodies (below drilled depths), as evidenced from the juvenile clasts in some of the breccias with felsic igneous matrix (Fig. 5A). At least two of the phreatomagmatic breccias appear to have intruded preferentially along the margins of the preexisting diorite intrusions (Fig. 2), suggesting this was a zone of weakness with increased permeability for magmatic-hydrothermal activity. The emplacement of the breccia with a felsic matrix diluted the metal grades (note effect on copper and gold contours in Fig. 4), whereas the breccia with a hydrothermal matrix is within the high-grade (>1 ppm Au) zone.

Several questions remain, including the following: How much metal, if any, that was precipitated during stage 2 was remobilized from deeper potassic-altered levels, rather than directly from the magmatic-hydrothermal source? How much metal in the Lepanto epithermal deposit was derived directly from a deep magmatic source versus remobilized from the porphyry Cu-Au deposit during the relatively late white-mica alteration overprint?

Alteration paragenesis of and metal introduction to porphyry Cu-Au deposits

Debates on the timing of copper introduction in porphyry deposits have long existed (Schwartz, 1947). In the case of Far Southeast, we have documented that copper and gold deposition was mostly associated with postbiotite stage 2 white-mica–chlorite-albite alteration, particularly that of the higher grades (>0.5 wt% Cu and >0.5 g/t Au). This is indicated by the spatial association of the high-grade ore shell and intense stage 2 alteration, by the large quantity of Cu sulfides in related lavender quartz veins, and by the abundance of paint veins with this stage and the subsequent white-mica alteration.

The dominance of postbiotite mineralization was also found to be the case at the gold-rich porphyry copper deposit of Batu Hijau, where Schirra et al. (2019, 2022) noted that the sulfides hosted by the A and B veins were deposited in crosscutting veinlets that reopened A and B veins, similar to C (paint) veins with narrow selvages of chlorite-sericite-albite (Clode et al., 1999). The albite-related alteration is not only post-A and B veins, it appears to also be associated with the event that deposited high copper and gold grades, like at Far Southeast. Garwin (2002) suggested that this sodic metasomatism at Batu Hijau was due to the presence of low-K tonalite intrusions, which promoted the formation of oligoclase ± albite alteration in the system. The dioritic intrusions at Far Southeast have a similar composition (App. Table A3) to the Batu Hijau tonalite, supporting the hypothesis that a mafic magmatic contribution was associated with the albite that formed during the main, high-grade stage of copper and gold mineralization.

Conclusions

At the young Far Southeast porphyry deposit (Arribas et al., 1995), shallow intrusion of diorite porphyry stocks into a ~2 Ma pyroclastic and porphyritic volcanic unit (Imbanguila) preceded the development of a magmatic-hydrothermal system, which by ~1.4 Ma formed biotite-magnetite alteration with sinuous veins of quartz and anhydrite plus deposition of ≤0.5% Cu and ≤0.5 g/t Au. Coupled with this early stage, acidic vapor condensates formed a lithocap (barren residual quartz core with quartz-alunite-kandite halo) at shallower depth, <1 km (Fig. 15A). As the system cooled, brittle veins of lavender quartz and anhydrite veins formed with alteration halos of white mica-chlorite-albite. This white mica is characterized by an Al-OH 2,200-nm peak position with higher SWIR wavelength than subsequent white-mica-only alteration, with means of 2,203 versus 2,197 nm, respectively (Fig. 11). Chalcopyrite and bornite paint veins also formed during these later stages, giving rise to the high-grade (~1 wt % Cu and ~1 g/t Au) mineralization of the porphyry deposit (Fig.

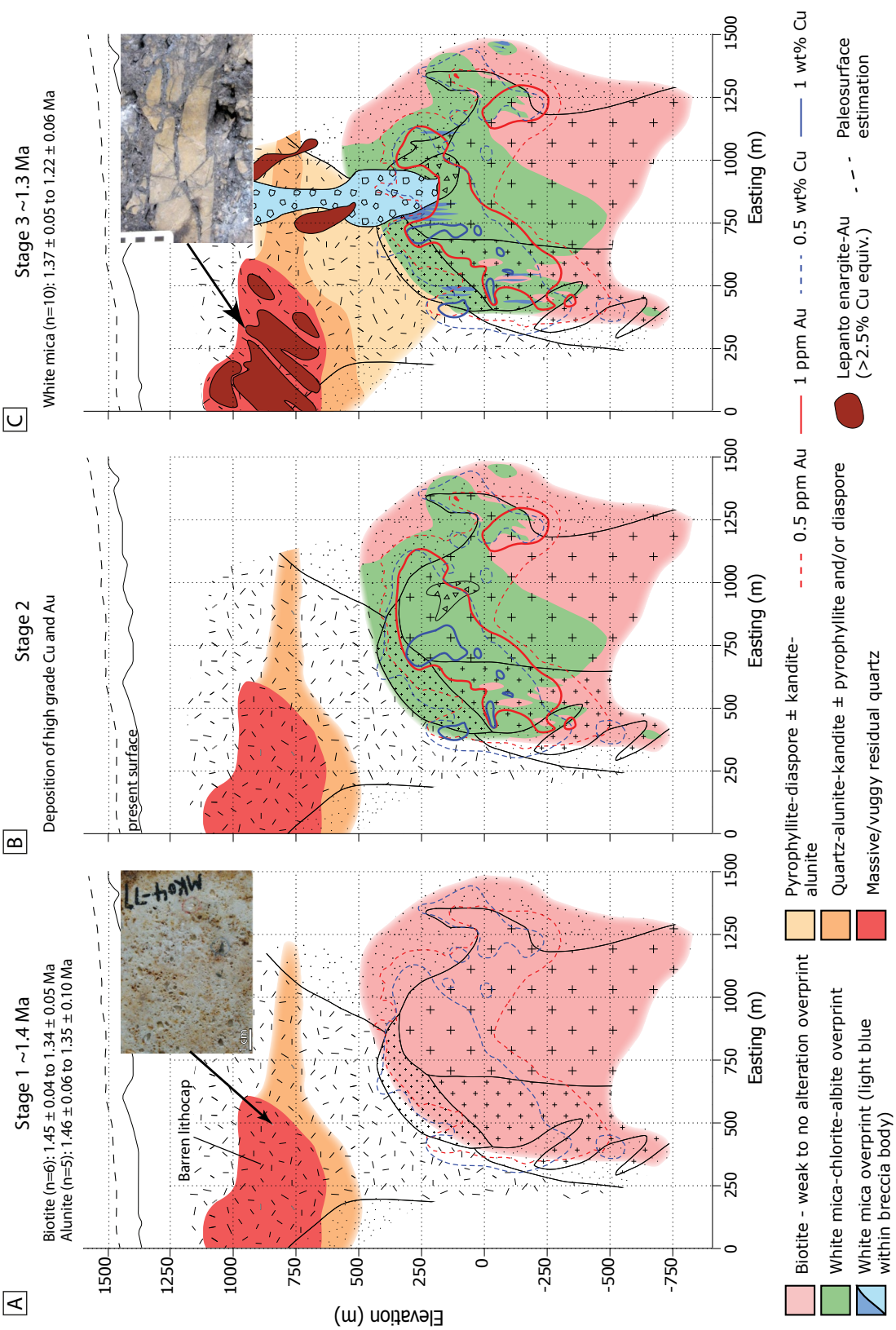

Fig. 15. Evolution of the Far Southeast porphyry system and Lepanto lithocap-hosted high-sulfidation deposit. A. ~1.4 Ma, biotite and barren lithocap formation at deep and shallow levels, respectively; lower-grade metal deposition at porphyry depths. Lithocap level, photograph of barren residual quartz with vuggy texture and minor alunite; 93.6% SiO_2, plus 1.8 ppb Au, 10 ppm Cu (pyrite oxidized). B. White-mica–chlorite-albite overprint of biotite and high-grade metal deposition at porphyry depths. Formation of hydrothermal breccia. C. ~1.3 Ma, formation of phreatomagmatic breccia bodies, white-mica-only overprint of porphyry, and transition up to aluminosilicate alteration to base of lithocap; potential remobilization of some metal from portions of the porphyry; ascent and cooling to the lithocap level, with high-sulfidation-state sulfide deposition, followed by intermediate-sulfidation-state sulfides and gold (Claveria, 2001). Photograph of brecciated massive and vuggy residual quartz, cemented by enargite mineralization. Detailed age ranges for biotite, alunite, and white-mica samples from Arribas et al. (1995).

15B). At shallower depths, in the transition to the base of the lithocap, subsequent cooling from white-mica stability led to the formation of aluminosilicate minerals (pyrophyllite ± diaspore ± dickite) with anhydrite plus high-sulfidation-state sulfides and pyrite veinlets (Fig. 15C). This later stage was likely the timing of metal transport to the lithocap, which formed the Lepanto enargite Au deposit (Hedenquist et al., 1998; Chang et al., 2011). There are at least three subvertical breccia bodies centered around the subvolcanic intrusive complex (Figs. 2, 15C); alteration of the breccia pipes is white mica only, with pyrite ± chalcopyrite.

The recognition of albite in the widespread white-mica–chlorite assemblage at Far Southeast (Gaibor et al., 2013; this study) is consistent with observations of postbiotite albite in other young, little-eroded porphyry deposits such as Batu Hijau (Clode et al., 1999; Garwin, 2002). This event (of an intermediate hydrothermal timing, postbiotite and pre-white mica-dominant) is associated with the highest concentrations of copper and gold and was a fundamental stage in the development of the Far Southeast deposit. We predict that on close examination albite, formed during high-grade metal introduction, will be found in other porphyry deposits, particularly those that are gold rich and associated with more mafic intrusions.

Acknowledgments

We acknowledge Bryan Yap, president of the Lepanto Consolidated Mining Company, and Frederick Louw, formerly president of Far Southeast Gold Resources Inc. (FSGRI), for permission to conduct this study, and Mr. Yap plus Gary Snow, vice president of exploration for Gold Fields Australia, for their permission to publish the results. We thank FSGRI for logistical support to MFC, ZC, AA, KK, and JWH during field visits to Lepanto, and Glacialle Tiu, formerly of FSGRI, for her generous contributions and assistance. This study was funded by James Cook University, Australia, the University of Geneva, Switzerland, Akita University, Japan, the SEG Foundation, and the Swiss Federal Social Insurance Office. We thank Dave Selby, Sebastian Meffre, and Fred Jourdan for the radiometric analyses, funded by FSGRI, Bill Chavez, John Muntean, and Richard Sillitoe, who provided constructive comments on early drafts, and Lisard Torró, Yi Sun, and David Cooke, whose careful manuscript reviews helped to clarify our presentation.

REFERENCES

Arif, J., and Baker, T., 2004, Gold paragenesis and chemistry at Batu Hijau, Indonesia: Implications for gold-rich porphyry copper deposits: Mineralium Deposita, v. 39, p. 523–535.

Arndt, N.T., Fontboté, L., Hedenquist, J.W., Kesler, S.E., Thompson, J.F., and Wood, D.G., 2017, Future global mineral resources: Geochemical Perspectives: v. 6, no. 1, p. 1–171.

Arribas, A., Jr., Hedenquist, J.W., Itaya, T., Okada, T., Concepción, R.A., and Garcia, J.S., Jr., 1995, Contemporaneous formation of adjacent porphyry and epithermal Cu-Au deposits over 300 ka in northern Luzon, Philippines: Geology, v. 23, p. 337–340.

Audétat, A., 2019, The metal content of magmatic-hydrothermal fluids and its relationship to mineralization potential: Economic Geology, v. 114, p. 1033–1056.

Audétat, A., and Simon, A.C., 2012, Magmatic controls on porphyry copper genesis: Society of Economic Geologists, Special Publication 16, p. 553–572.

Barrier, E., Huchon, P., and Aurelio, M., 1991, Philippine fault: A key for Philippine kinematics: Geology, v. 19, p. 32–35.

Bouzari, F., and Clark, A.H., 2006, Prograde evolution and geothermal affinities of a major porphyry copper deposit: The Cerro Colorado hypogene protore, I Región, northern Chile: Economic Geology, v. 101, p. 95–134.

Bunce, M., 2015, Gold deportment and trace-element content of copper sulphides of the Far Southeast porphyry copper-gold deposit, Philippines: Unpublished B.Sc. Honours thesis, Ottawa, Ontario, University of Ottawa, 105 p.

Chang, Z., Hedenquist, J.W., White, N.C., Cooke, D.R., Roach, M., Deyell, C.L., Garcia, J., Jr., Gemmell, J.B., McKnight, S., and Cuison, A.L., 2011, Exploration tools for linked porphyry and epithermal deposits: Example from the Mankayan intrusion-centered Cu-Au district, Luzon, Philippines: Economic Geology, v. 106, p. 1365–1398.

Claveria, R.J.R., 2001, Mineral paragenesis of the Lepanto copper and gold and the Victoria gold deposits, Mankayan mineral district, Philippines: Resource Geology, v. 51, p. 97–106.

Clode, C., Proffett, J., Mitchell, P., and Munajat, I., 1999, Relationships of intrusion, wall-rock alteration and mineralization in the Batu Hijau copper-gold porphyry deposit: PACRIM '99 Congress, Bali, Indonesia, October 10–13, 1999, Proceedings, p. 485–498.

Concepción, R.A., and Cinco, J.C., Jr., 1989, Geology of the Lepanto-Far Southeast gold-rich copper deposit: International Geological Congress, Washington, D.C., 1989, Proceedings, v. 1, p. 319–320, and preprint, 46 p.

Cooke, D.R., Hollings, P., and Walshe, J.L., 2005, Giant porphyry deposits: Characteristics, distribution, and tectonic controls: Economic Geology, v. 100, p. 801–818.

Doublier, M.P., Roache, T., and Potel, S., 2010, Short-wavelength infrared spectroscopy: A new petrological tool in low-grade to very low-grade pelites: Geology, v. 38, no. 11, p. 1031–1034.

Einaudi, M.T., Hedenquist, J.W., and Inan, E.E., 2003, Sulfidation state of fluids in active and extinct hydrothermal systems: Transitions from porphyry to epithermal environments: Society of Economic Geologists, Special Publication 10, p. 285–314.

Fournier, R.O., 1985, The behavior of silica in hydrothermal solutions: Reviews in Economic Geology, v. 2, p. 45–61.

Frey, M., 1987, Very low-grade metamorphism of clastic sedimentary rocks, *in* Frey, M., ed., Low temperature metamorphism: New York, Chapman and Hall, p. 9–58.

Gaibor, A., Dunkley, P., Wehrle, A., Lesage, G., Den Boer, D., and Conde, F., 2013, The discovery and understanding of the Far Southeast copper-gold porphyry, Luzon, Philippines: Case Histories of Discovery, NewGenGold 2013, Perth, November 26–27, 2013, Proceedings, p. 233–247.

Garcia, J.S., Jr., 1991, Geology and mineralization characteristics of the Mankayan mineral district, Benguet, Philippines: Geological Survey of Japan, Report 277, p. 21–30.

Garwin, S., 2002, The geologic setting of intrusion-related hydrothermal systems near the Batu Hijau porphyry copper-gold deposit, Sumbawa, Indonesia: Society of Economic Geologists, Special Publication 9, p. 333–366.

Gold Fields, 2019, Resources and mineral reserves supplement to the integrated annual report: www.goldfields.com/far-southeast-philippines.php, accessed March 4, 2021.

Gonzalez, A.G., 1959, Geology and genesis of the Lepanto copper deposit, Mankayan, Mountain province, Philippines: Unpublished Ph.D. dissertation, Stanford, California, Stanford University, 102 p.

Gregory, M.J., 2017, A fluid inclusion and stable isotope study of the Pebble porphyry copper-gold-molybdenum deposit, Alaska: Ore Geology Reviews, v. 80, p. 1279–1303.

Gregory, M.J., Lang, J.R., Gilbert, S., and Hoal, K.O., 2013, Geometallurgy of the Pebble porphyry copper-gold-molybdenum deposit, Alaska: Implications for gold distribution and paragenesis: Economic Geology, v. 108, p. 463–482.

Gustafson, L.B., and Hunt, J.P., 1975, The porphyry copper deposit at El Salvador, Chile: Economic Geology, v. 70, p. 857–912.

Hedenquist, J.W., and Arribas, A., 2022, Exploration implications of multiple formation environments of advanced argillic minerals: Economic Geology, v. 117, p. 609–643, doi: 10.5382/econgeo.4880.

Hedenquist, J.W., and Taran, Y.A., 2013, Modeling the formation of advanced argillic lithocaps: Volcanic vapor condensation above porphyry intrusions: Economic Geology, v. 108, p. 1523–1540.

Hedenquist, J.W., Arribas, A., and Reynolds, T.J., 1998, Evolution of an intrusion-centered hydrothermal system; Far Southeast-Lepanto porphyry and epithermal Cu-Au deposits, Philippines: Economic Geology, v. 93, p. 373–404.

Hedenquist, J.W., Arribas, A., and Gonzalez-Urien, E., 2000, Exploration for epithermal gold deposits: Reviews in Economic Geology, v. 13, p. 45–77.

Hedenquist, J.W., Arribas, A., and Aoki, M., 2017, Zonation of sulfate and sulfide minerals and isotopic composition in the Far Southeast porphyry and Lepanto epithermal Cu-Au deposits, Philippines: Resource Geology, v. 67, p. 174–196.

Hemley, J.J., and Jones, W.R., 1964, Chemical aspects of hydrothermal alteration with emphasis on hydrogen metasomatism: Economic Geology, v. 59, p. 538–569.

Hemley, J.J., Montoya, J.W., Marinenko, J.W., and Luce, R.W., 1980, Equilibria in the system Al_2O_3-SiO_2-H_2O and some general implications for alteration/mineralization processes: Economic Geology, v. 75, p. 210–228.

Henley, R.W., and McNabb, A., 1978, Magmatic vapor plumes and groundwater interaction in porphyry copper emplacement: Economic Geology, v. 73, p. 1–20.

Hollings, P., Wolfe, R., Cooke, D.R., and Waters, P.J., 2011, Geochemistry of Tertiary igneous rocks of northern Luzon, Philippines: Evidence for a back-arc setting for alkalic porphyry copper-gold deposits and a case for slab roll-back?: Economic Geology, v. 106, p. 1257–1277.

Kouzmanov, K., and Pokrovski, G.S., 2012, Hydrothermal controls on metal distribution in porphyry Cu (-Mo-Au) systems: Society of Economic Geologists, Special Publication 16, p. 573–618.

Landtwing, M.R., Pettke, T., Halter, W.E., Heinrich, C.A., Redmond, P.B., Einaudi, M.T., and Kunze, K., 2005, Copper deposition during quartz dissolution by cooling magmatic-hydrothermal fluids: The Bingham porphyry: Earth and Planetary Science Letters, v. 235, p. 229–243.

Lang, J.R., and Gregory, M.J., 2012, Magmatic-hydrothermal-structural evolution of the giant Pebble porphyry Cu-Au-Mo deposit with implications for exploration in southwest Alaska: Society of Economic Geologists, Special Publication 16, p. 167–186.

Leys, C.A., Schwarz, A., Cloos, M., Sugeng Widodo, J., Kyle, R., and Sirait, J., 2019, Grasberg copper-gold-(molybdenum) deposit: Product of two overlapping porphyry systems: Society of Economic Geologists, Special Publication 23, p. 599–620.

Lindgren, W., 1933, Mineral deposits, 4th ed.: New York, McGraw-Hill, 930 p.

Lowell, J.D., and Guilbert, J.M., 1970, Lateral and vertical alteration-mineralization zoning in porphyry ore deposits: Economic Geology, v. 65, p. 373–408.

Maleterre, P., 1989, Histoire sédimentaire, magmatique, tectonique et métallogénique d'un arc cénozoïque déformé en régime de transpression: la Cordillère Centrale de Luzon, à l'extrémité de la faille philippine, sur les transects de Baguio et de Cervantes-Bontoc: contexte structural et géodynamique des minéralisations épithermales aurifères: Doctoral dissertation, Brest, France, Université de Bretagne Occidentale, 367 p.

Masterman, G.J., Cooke, D.R., Berry, R.F., Walshe, J.L., Lee, A.W., and Clark, A.H., 2005, Fluid chemistry, structural setting, and emplacement history of the Rosario Cu-Mo porphyry and Cu-Ag-Au epithermal veins, Collahuasi district, northern Chile: Economic Geology, v. 100, p. 835–862.

Meyer, C., and Hemley, J.J., 1967, Wall-rock alteration, *in* Barnes, H.L., ed., Geochemistry of hydrothermal ore deposits: New York, Holt, Rinehart, and Winston, p. 166–235.

Ossandón C., G., Fréraut C., R., Gustafson, L.B., Lindsay, D.D., and Zentilli, M., 2001, Geology of the Chuquicamata mine: A progress report: Economic Geology, v. 96, p. 249–270.

Padilla-Garza, R.A., Titley, S.R., and Pimentel B., F., 2001, Geology of the Escondida porphyry copper deposit, Antofagasta region, Chile: Economic Geology, v. 96, p. 307–324.

Padilla-Garza, R.A., Titley, S.R., and Eastoe, C.J., 2004, Hypogene evolution of the Escondida porphyry copper deposit, Chile: Society of Economic Geologists, Special Publication 11, p. 141–165.

Perelló, J., Brockway, H., and Martini, R., 2004, Discovery and geology of the Esperanza porphyry copper-gold deposit, Antofagasta region, northern Chile: Society of Economic Geologists Special, Publication 11, p. 167–186.

Proffett, J.M., 2003, Geology of the Bajo de la Alumbrera porphyry copper-gold deposit, Argentina: Economic Geology, v. 98, p. 1535–1574.

Queano, K.L., Ali, J.R., Milsom, J., Aitchison, J.C., and Pubellier, M., 2007, North Luzon and the Philippine Sea Plate motion model: Insights following paleomagnetic, structural, and age-dating investigations: Journal of Geophysical Research: Solid Earth, v. 112, 44 p.

Redmond, P.B., and Einaudi, M.T., 2010, The Bingham Canyon porphyry Cu-Mo-Au deposit. I. Sequence of intrusions, vein formation, and sulfide deposition: Economic Geology, v. 105, p. 43–68.

Redmond, P.B., Einaudi, M.T., Inan, E.E., Landtwing, M.R., and Heinrich, C.A., 2004, Copper deposition by fluid cooling in intrusion-centered systems: New insights from the Bingham porphyry ore deposit, Utah: Geology, v. 32, p. 217–220.

Reed, M., Rusk, B., and Palandri, J., 2013, The Butte magmatic-hydrothermal system: One fluid yields all alteration and veins: Economic Geology, v. 108, p. 1379–1396.

Rusk, B., and Reed, M., 2002, Scanning electron microscope-cathodoluminescence analysis of quartz reveals complex growth histories in veins from the Butte porphyry copper deposit, Montana: Geology, v. 30, p. 727–730.

Schirra, M., Driesner, T., and Heinrich, C.A., 2019, Relative timing of sulfide precipitation at the Batu Hijau porphyry Cu-Au deposit, Sumbawa, Indonesia: Society for Geology Applied to Mineral Deposits (SGA) Biennial Meeting, 15th, Glasgow, 2019, Proceedings, v. 3, p. 1009–1012.

Schirra, M., Laurent, O., Zwyer, T., Driesner, T., and Heinrich, C.A., 2022, Fluid evolution at the Batu Hijau porphyry Cu-Au deposit, Indonesia: Hypogene sulfide precipitation from a single-phase aqueous magmatic fluid during chlorite–white-mica alteration: Economic Geology, v. 117, p. 979–1012.

Schwartz, G.M., 1947, Hydrothermal alteration in the "porphyry copper" deposits: Economic Geology, v. 42, p. 319–352.

Seedorff, E., Dilles, J., Proffett, J.M., Einaudi, M.T., Zurcher, L., Stavast, W.J.A., Johnson, D.A., and Barton, M., 2005, Porphyry deposits: Characteristics and origin of hypogene features: Economic Geology 100th Anniversary Volume, p. 251–298.

Seedorff, E., Barton, M.D., Stavast, W.J.A., and Maher, D.J., 2008, Root zones of porphyry systems: Extending the porphyry model to depth: Economic Geology, v. 103, p. 939–956.

Shock, E.L., Helgeson, H.C., and Sverjensky, D.A., 1989, Calculation of the thermodynamic and transport properties of aqueous species at high pressures and temperatures: Standard partial molal properties of inorganic neutral species: Geochimica et Cosmochimica Acta, v. 53, p. 2157–2183.

Sillitoe, R.H., 1983, Enargite-bearing massive sulfide deposits high in porphyry copper systems: Economic Geology, v. 78, p. 348–352.

——1995, Exploration of porphyry copper lithocaps: Australian Institute of Mining and Metallurgy, PacRim Congress, Auckland, New Zealand, 1995, Proceedings, p. 527–532.

——1999, Styles of high-sulphidation gold, silver and copper mineralization in the porphyry and epithermal environments: Australian Institute of Mining and Metallurgy, PacRim '99, Bali, Indonesia, October 10–13, 1999, Proceedings, p. 29–44.

——2010, Porphyry copper systems: Economic Geology, v. 105, p. 3–41.

Sillitoe, R.H., and Angeles, C.A., Jr., 1985, Geological characteristics and evolution of a gold-rich porphyry copper deposit at Guinaoang, Luzon, Philippines: Asian Mining '85, Manila, Philippines, February 11–14, Proceedings, p. 15–26.

Sillitoe, R.H., and Gappe, I.M., Jr., 1984, Philippine porphyry copper deposits: Geologic setting and characteristics: United Nations Economic and Social Commission for Asia and the Pacific (ESCAP) CCOP Technical Publication 14, 89 p.

Sillitoe, R.H., and Hedenquist, J.W., 2003, Linkages between volcanotectonic settings, ore-fluid compositions, and epithermal precious metal deposits: Society of Economic Geologists, Special Publication 10, p. 315–343.

Stefanova, E., Driesner, T., Zajacz, Z., Heinrich, C.A., Petrov, P., and Vasilev, Z., 2014, Melt and fluid inclusions in hydrothermal veins: The magmatic to hydrothermal evolution of the Elatsite porphyry Cu-Au deposit, Bulgaria: Economic Geology, v. 109, p. 1359–1381.

Tsuruoka, S., Monecke, T., and Reynolds, T.J., 2021, Evolution of the magmatic-hydrothermal system at the Santa Rita porphyry Cu deposit, New Mexico, USA: Importance of intermediate-density fluids in ore formation: Economic Geology, v. 116, p. 1267–1284.

Uribe-Mogollon, C., and Maher, K., 2018, White mica geochemistry of the Copper Cliff porphyry Cu deposit: Insights from a vectoring tool applied to exploration: Economic Geology, v. 113, p. 1269–1295.

Watanabe, Y., and Hedenquist, J.W., 2001, Mineralogic and stable isotope zonation at the surface over the El Salvador porphyry copper deposit, Chile: Economic Geology, v. 96, p. 1775–1797.

Watanabe, Y., Sato, R., and Sulaksono, A., 2018, Role of potassic alteration for porphyry Cu mineralization: Implication for the absence of porphyry Cu deposits in Japan: Resource Geology, v. 68, p. 195–207.

Weis, P., Driesner, T., and Heinrich, C.A., 2012, Porphyry-copper ore shells form at stable pressure-temperature fronts within dynamic fluid plumes: Science, v. 338, p. 1613–1616.

Wright, J.V., Smith, A.L., and Self, S., 1980, A working terminology of pyroclastic deposits: Journal of Volcanology and Geothermal Research, v. 8, p. 315–336.

Michael F. Calder has conducted research on magmatic-hydrothermal deposits in Armenia and the Philippines, affiliated with the University of Geneva, Switzerland, and James Cook University, Australia. After working in an energy consulting firm, he has focused on ore deposit research and is based in Geneva. He acknowledges the importance of metals to help decarbonize the world economy. Recently, he has been involved in Ore Deposits Hub, an online economic geology communication platform. He enjoys traveling, arts and culture, the outdoors, and hiking in the mountains.